Nano-crystal domains in Co-based fcc(111) epitaxial magnetic junctions and their impact on tunnel magnetoresistance

Cong He[1,*], Keisuke Masuda[1], Jieyuan Song[1,2], Thomas Scheike[1], Zhenchao Wen[1], Yoshio Miura[1], Tadakatsu Ohkubo[1], Kazuhiro Hono[1], Seiji Mitani[1,2], and Hiroaki Sukegawa[1]

[1] National Institute for Materials Science (NIMS), Tsukuba 305-0047, Japan
[2] Graduate School of Science and Technology, University of Tsukuba, Tsukuba 305-8577, Japan

*Corresponding author
Email address: he.cong@nims.go.jp (Cong He)

Abstract

Nano-crystal domain structures formed in a MgO barrier and their effects on tunnel magnetoresistance (TMR) in epitaxial fcc-$Co_{90}Fe_{10}$ (CoFe)(111)/MgO(111)/CoFe(111) magnetic tunnel junctions (MTJs) have been systematically studied using scanning transmission electron microscopy and first-principles calculations. These domains are widely distributed in the (111)-textured MgO layer, being different from conventional bcc-CoFe/MgO(001)-based MTJs. The (111)-texture is formed by extension of {111} planes through several adjacent MgO domains. Three types of orientation relationships (ORs) between CoFe and MgO are identified, including cube-on-cube type (Type-1), twin-like type (Type-2), and unexpected type (Type-3), with a similar volume fraction. Crystallographic analysis indicated that Type-2 OR is a variant of Type-1 OR, triggered by different stacking orders of MgO(111) planes, while Type-3 OR is formed by a 30° in-plane rotation of MgO lattice relative to Type-1 OR. Due to the large in-plane lattice mismatch (19.6%) between Co(111) and MgO(111) in Type-1 and Type-2 ORs, Type-3 OR (mismatch 3.4%) can be stabilized. First-principles calculations uncovered that the theoretical TMR ratio of the MgO(111) MTJ with Type-3 OR is ~2 orders of magnitude smaller than that with Type-1 and Type-2 ORs. The small contribution of Type-3 OR to the transport reasonably interprets why the experimental TMR ratio (~37%) is much lower than the theoretical value (~2100%) in the Co/MgO/Co(111) MTJ. This study has revealed the nano-crystal domain formation unique to the fcc-CoFe/MgO(111) MTJs, indicating that controlling the nano-crystal domains (e.g., lattice optimization by atomic doping) can be a guiding principle to develop MgO(111)-based epitaxial MTJs and related heterostructure devices.

Keywords: Epitaxial growth; Nano-crystal domains; Magnetic tunnel junctions; Tunneling magnetoresistance; Microstructure

1. Introduction

A magnetic tunnel junction (MTJ) consists of a trilayer structure where a very thin insulating oxide layer (barrier) is sandwiched between two ferromagnets (FMs). The relative orientation change from parallel (P) to antiparallel (AP) alignment between the magnetizations of the FM electrodes leads to a change in the tunneling current through the insulating barrier, resulting in a low- and high-resistance state, respectively. This change in orientation-dependent resistance is called the tunnel magnetoresistance (TMR) effect. In the past two decades, this effect has been extensively investigated both experimentally and theoretically using (001)-oriented MTJs, i.e., bcc-FM(001)/fcc-based oxide barrier(001)/bcc-FM(001) structures, such as Fe/MgO/Fe(001) [1-9], bcc-Co/MgO/Co(001) [10, 11], CoFe(B)/MgO/CoFe(B)(001) [12-15], and Fe/$MgAl_2O_4$/Fe(001) MTJs [8, 16, 17]. Especially, the polycrystalline CoFeB/MgO/CoFeB MTJ has been used in most practical MTJs, such as non-volatile magnetoresistive random access memories (MRAMs) and read heads of hard disk drives (HDDs). In the (001)-oriented MTJs, the spin-dependent coherent tunneling effect of Δ_1 Bloch states leads to significant spin-filtering through the MgO barrier, resulting in giant TMR ratios compared with amorphous barrier-based MTJs such as AlO_x [1, 2, 5, 7, 10, 18, 19]. To date, the largest room temperature (RT) TMR ratio of 631% has been achieved using a CoFe/MgO/CoFe(001) MTJ [15].

However, for the scaling down of MRAM cells less than a few 10 nm scale, a strong perpendicular magnetic anisotropy (PMA) that can withstand the high temperatures of the semiconductor back-end process of 350–400 °C is required for MTJs in addition to a large TMR ratio [6, 20-24]. It has been reported that close-packed plane of fcc(111) or hcp(0001) oriented noble metal-based multilayers and superlattices could be used to ensure the strong PMA as hard layers of a perpendicularly magnetized MTJ (p-MTJ) for MRAMs: e.g., Co/Pt [25-31], CoFe/Pt [32], Co/Pd [25, 33], and CoFe/Pd [34, 35]. However, such materials with the fcc(111)-based orientation [21, 34, 36] are unfavorable for direct combination with the (001)-oriented MTJ trilayer, i.e., CoFeB/MgO/CoFeB, due to the difference in their in-plane lattice structures and lattice constants, which hinders the flexible design and thermal stability of p-MTJs. For example, an ultrathin (0.1~0.3 nm thick) texture-breaking layer, such as Ta and W, is generally necessary between the PMA multilayers and the CoFeB layer to suppress the effect of the (111) lattices on the (001) trilayer [29-31]. If fully fcc(111) oriented MTJ trilayers compatible with such fcc-based PMA layers are developed, we will expand the range of the p-MTJ stacking design that can withstand high-temperature processes.

In a recent theoretical study, Masuda *et al.* [37] reported a large TMR ratio of ~2100% in a fcc-Co(111)/MgO(111)/Co(111) MTJ trilayer with a cube-on-cube orientation relationship (OR) between the Co layers and the MgO barrier (hereafter, referred to as Type-1 OR, i.e., Co(Pt)(111)[$\bar{1}$10] // MgO(111)[$\bar{1}$10]). They attributed the large TMR ratio in the (111)-oriented MTJ to the interfacial resonance effect of the *d-p* antibonding states [37], which is radically different from the coherent tunneling mechanism of the bulk Δ_1 states in the conventional Fe/MgO/Fe(001) based MTJs. However, their calculations assumed that the large strain of ~19.6% at the Co/MgO interface was elastically relaxed to construct their supercell. Therefore, it is of great interest to experimentally clarify the actual OR and lattice matching at the fcc-Co/MgO interfaces in such a (111)-oriented MTJ with a large theoretical mismatch. So far, the epitaxial growth of fcc(111)-oriented Co [38] and CoPt [36, 39] films on MgO(111) has been experimentally reported to have a cube-on-cube OR. Additionally, the thermally stable Co-based superlattices were shown to retain a large PMA and an fcc(111) texture after post-annealing [21, 34]. Recently, Song *et al.* [40] demonstrated a TMR effect in fcc(111)-stacked $Co_{90}Fe_{10}$ (CoFe)/Mg_4Al-O_x (MAO)/$Co_{90}Fe_{10}$ structure as a new class of epitaxial MTJ. In the

MTJ stack, the large lattice mismatch between the fcc-CoFe and MAO was effectively relaxed by the introduction of periodic misfit dislocations, forming the relatively flat barrier interfaces. However, the observed TMR ratio was 37% at RT (47% at 10 K), which is about two orders of magnitude smaller than the theoretical value in a similar structure, i.e., Co/MgO/Co(111). Further microstructural analysis using transmission electron microscopy (TEM) and theoretical calculations are necessary to elucidate the origin of the large discrepancy between the experiment and theory.

In the article, we performed a systematic microstructural characterization of the fully epitaxial CoFe/MgO/CoFe(111) MTJ using atomic resolution scanning transmission electron microscopy (STEM) imaging. In addition, we calculated the spin-dependent transport properties based on the observed atomic structures. The STEM analysis revealed that there are abundant MgO nano-crystal domains within the (111)-textured MgO barrier. Three types of ORs between CoFe(111) and MgO(111) atomic planes are detected: a cube-on-cube type (Type-1 OR), a twin-like type (Type-2 OR), and an unexpected type (Type-3 OR). We found that the Type-2 OR is formed as a variant of the Type-1 OR (stacking of different MgO(111) planes), and the Type-3 OR is formed by a 30° in-plane rotation of the Type-1 OR. The formation of these three ORs is rationalized by detailed crystallographic analysis. The first-principles calculations reasonably explained the small experimental TMR ratios by considering the unexpected Type-3 OR, which significantly suppresses the magnitude of the TMR ratio of the (111)-MTJ. Finally, possible strategies, such as atomic doping, are proposed to rationally design future Co-based (111)-oriented MTJs and thus improve the TMR ratio.

2. Methods

The MTJ multilayers were deposited on single-crystalline α-Al_2O_3 (0001) (basal-plane sapphire) substrates using magnetron sputtering in an ultrahigh vacuum sputtering system (ULVAC, Inc.) at a base pressure of ~4×10^{-7} Pa. Prior to the deposition process, the substrates were annealed at 1000 °C for 1 hour in a muffle furnace to smooth the surface and remove surface contaminants. The stacking structure is: Al_2O_3//Ru (40)/$Co_{90}Fe_{10}$ (CoFe, 20)/Mg (0.5)/$MgAl_4$-O_x (3)/CoFe (5)/Ru (0.75)/$Co_{50}Fe_{50}$ (2.2)/IrMn (10)/Ru (10) (numbers in nm), as shown in the schematic illustration in Fig. 1a. Detailed deposition procedures can be found in Ref. [40]. Since fcc- and hcp-Co could coexist in thin films at RT [38, 41], 10 at.% Fe was added to Co to acquire a single fcc phase. The previous analysis revealed that the Al concentration of the layer deposited using electron-beam evaporation from the Mg_4Al-O_x pellet was almost negligible [40]. Thus, hereafter we referred this layer as a MgO barrier. After deposition, the films were magnetically annealed at 300 °C for 2 h in a high vacuum chamber under a magnetic field of 0.7 T. The multilayers were subsequently patterned into 39 μm^2 elliptical junctions using photolithography and Ar ion beam etching. The TMR ratio was characterized by a DC four-probe method at RT. The TMR ratio was defined by $(R_{AP} - R_P) / R_P \times 100\%$, where R_{AP} and R_P represent the resistance of the AP and P state, respectively.

Cross-sectional scanning transmission electron microscopy (STEM) samples were prepared by the focused ion beam (FIB) milling technique using a Ga^+ source. A low energy of 2 keV was utilized at the final cleaning step to remove the damaged and Ga^+ implanted layer caused by high energy milling in the early stage. STEM observations, energy dispersive X-ray spectroscopy (EDS) and nano-beam electron diffraction (NBED) analyses were performed using a Cs-corrected FEI Titan G2 80–200 ChemiSTEM operated at 200 kV. To reveal the atomic-scale details within the

CoFe/MgO/CoFe trilayer, high-angle annular dark-field STEM (HAADF-STEM) (Z-contrast) imaging is not used here due to a large atomic number difference in the trilayer; instead, annular dark-field STEM (ADF-STEM) imaging is adopted where the use of a large camera length (255–410 mm) generates diffraction contrast in the corresponding images. Drift-corrected EDS maps were collected in Bruker Esprit analysis system where image drift during data collection was automatically corrected. EDS line profiles were quantified by the Cliff–Lorimer analysis method.

All the theoretical calculations in this study are based on the density-functional theory (DFT) and an MTJ structure with Co/MgO/Co(111), instead of the CoFe/MAO/CoFe(111) for simplicity. We first conducted a structure optimization of the Co/MgO/Co(111) supercell (Fig. 8a) using the Vienna *ab-initio* simulation program (VASP) [42]. The electronic exchange-correlation energy was described using the generalized gradient approximation (GGA) [43]. The projector augmented wave (PAW) pseudopotential [44] was used to treat the effect of core electrons properly. The cutoff energy was set as 500 eV and the Brillouin-zone integration was performed using 13 × 13 × 1 k points. The *a*-axis (Co[$1\bar{1}0$]) and *b*-axis (Co[$01\bar{1}$]) lengths of the supercell were fixed to be $a = b = \sqrt{2}a_{\text{fcc-Co}}$ where $a_{\text{fcc-Co}} = 0.352$ nm, and atomic positions in the supercell were relaxed along the *c* direction (Co[111]). Using the optimized supercell, we calculated the TMR ratio based on the DFT and Landauer formula with the aid of the PWCOND code [45] in the QUANTUM ESPRESSO package [46, 47]. In the DFT calculation, the GGA and ultrasoft pseudopotentials [48] were used. The correspongding cutoff energies for the wave functions and the charge density were set as 45 and 450 Ry, respectively, and 13 × 13 × 1 **k** points were utilized for the Brillouin-zone integration. Since there is a translational symmetry in the *ab* plane of the system, the scattering state can be assigned by an in-plane wave vector $\mathbf{k}_{\parallel} = (k_x, k_y)$. For each $\mathbf{k}_{\parallel}$ and spin index, we solved the scattering equation derived under the condition where the wave function and its derivative of the supercell connect to those of the electrodes [45, 49]. Based on the acquired transmittance, the conductance was calculated through the Landauer formula. These calculations for both P and AP states of electrodes give the wave-vector-resolved conductances: $G_{\text{P},\uparrow}(\mathbf{k}_{\parallel})$, $G_{\text{P},\downarrow}(\mathbf{k}_{\parallel})$, $G_{\text{AP},\uparrow}(\mathbf{k}_{\parallel})$, and $G_{\text{AP},\downarrow}(\mathbf{k}_{\parallel})$, where ↑ (↓) represents the up-spin (down-spin) channel. We calculated the averaged conductances as, e.g., $G_{\text{P},\uparrow} = \Sigma_{\mathbf{k}\parallel} G_{\text{P},\uparrow}(\mathbf{k}_{\parallel}) / N$, where N is the sampling number of $\mathbf{k}_{\parallel}$ points and was set as 150 × 150 = 2250. The TMR ratio was thus calculated by $(G_{\text{P}} - G_{\text{AP}}) / G_{\text{AP}} \times 100\%$, the same definition as for the experiments $[(R_{\text{AP}} - R_{\text{P}}) / R_{\text{P}} \times 100\%]$. More detailed information can be found in the previous works [37, 50].

3. Results

Figure 1b displays the measured TMR ratios and electrical resistance as a function of in-plane magnetic field (*H*) at 300 K for the MTJ with a MgO barrier of 3 nm. The upper-right inset of Fig. 1b is a minor R-H loop, showing a clear magnetization reversal of the bottom CoFe. The MTJ shows a TMR ratio of 36.8%, which is comparable with the value in the MgO barrier of 2.5 nm [40]. The TMR ratio is nearly two orders of amplitude lower than the theoretical one in Co/MgO/Co(111) (~2100%) [37]. To understand the origin of the substantial discrepancy between the experimental and theoretical TMR ratios, we first performed a systematic microstructure analysis of the CoFe/MgO/CoFe MTJ.

The low-magnification ADF-STEM image in Fig. 2a shows the cross-sectional microstructure of the CoFe/MgO/CoFe MTJ, with the electron beam direction parallel to [$\bar{1}100$] of Al_2O_3 substrate. The layered structure and rather flat interfaces are revealed, indicating the successful preparation of a

high-quality thin multilayer which is critical to a high-performance MTJ. The elemental EDS maps in Fig. 2b suggest that each element is homogeneously distributed in their designed layers, except that a small amount of Fe atoms have segregated to the lower and upper CoFe/MgO interfaces, as confirmed by the quantitative EDS line profile of Fe in Fig. 2c (Fe enrichments at the interfaces are marked with black arrows). The elemental line profiles also show that the measured stoichiometric ratio of each element in each layer agrees well with the value in designed materials, e.g., 90 : 10 for the CoFe layers and 50 : 50 for the MgO barrier. The detection of the Fe segregation at the interface should be ascribed to the better chemical affinity of Fe with O than that of Co [51]. Here, the addition of 10 at% Fe to Co is intended to maintain the fcc structure of the electrode by suppressing hcp-Co formation. It is speculated that the effect of such a small Fe addition on the TMR ratio should be negligible. Therefore, the structure can be essentially treated as the Co/MgO/Co structure assumed in our later theoretical calculations.

A high-magnification ADF-STEM image in Fig. 3a shows the atomic-resolution microstructure close to the trilayer of CoFe/MgO/CoFe, where CoFe has an A1|fcc structure. The image is recorded along the direction of CoFe[$\bar{1}$ 10] // α-Al_2O_3[$\bar{1}$ 100] (epitaxial growth is achieved between CoFe(111)[$\bar{1}$10], Ru(0001)[$\bar{1}2\bar{1}0$] and α-Al_2O_3(0001)[$\bar{1}$100] [36]). Figure 3b shows that the NBED patterns collected from the bottom CoFe, MgO barrier and upper CoFe can be indexed along the CoFe[$\bar{1}$10] and MgO[$\bar{1}$10] zone axes, verifying the cube-on-cube OR between fcc-CoFe and rocksalt-MgO, i.e., CoFe(111)[$\bar{1}$10] // MgO(111)[$\bar{1}$10] which is commonly observed at fcc-metal/fcc-metal and MgO/fcc-metal interfaces [52-54]. Here, the cube-on-cube orientation is defined as Type-1 OR, with the region in the MgO barrier that has this type of OR defined as Type-1 domain and the corresponding lattice match at the CoFe/MgO interface defined as Type-1 lattice match. This Type-1 OR also indicates the successful achievement of epitaxial growth of (111) orientation in the bottom CoFe, MgO and upper CoFe layers of this MTJ. However, the atomic-scale image in Fig. 3a implies that the MgO barrier is not single-crystalline and the crystal domain size of MgO in the barrier that has a cube-on-cube orientation with CoFe is only ~5 nm in diameter. There also appears to be a slight in-plane rotation with respect to the normal direction of the film, as shown in Fig. 3a where the right MgO crystal grain has extended its {111} atomic planes into the left one. Moreover, the quality of the upper CoFe layer seems to have been affected due to the in-plane rotation in MgO, with a poorer quality than that of the bottom CoFe. Figure 3c illustrates the related lattice matching scenario for Type-1 OR at the CoFe/MgO interface. The close-packed planes of CoFe{111} and MgO{111} are marked by ABCABC and $A_1B_1C_1A_1B_1C_1$, respectively. The stacking sequence of the close-packed planes at the CoFe/MgO interface is …$ABCA_1B_1C_1$... for a Type-1 lattice match. The ADF-STEM image in Fig. 3d displays another cube-on-cube oriented region in which the MgO grain size has a larger value of ~13 nm. Again, the stacking sequence at the CoFe/MgO interface is …$ABCA_1B_1C_1$... Based on the NBED pattern in Fig. 3b and the atomic image in Fig. 3d, the MgO barrier has a rocksalt structure and lattice parameter of a = 0.420 nm which is the same as the MgO bulk value (a = 0.421 nm). The lattice mismatch at the CoFe/MgO interface is calculated to be 19.6% (see 4.1). The Fourier-filtered image in Fig. 3e corresponds to the region marked with a dashed frame in Fig. 3d. Clearly, every six CoFe(11$\bar{1}$) planes are well matched to five MgO(11$\bar{1}$) planes, leading to the formation of interfacial misfit dislocations that are periodically spaced by an interval of every six CoFe(11$\bar{1}$) planes (~1.3 nm).

Figure 4 shows the Type-2 domain having a twin-like orientation with the bottom CoFe. Here, this orientation is defined as Type-2 OR and the region in the MgO barrier having this orientation is called Type-2 domain. As shown in the atomic ADF-STEM image taken along the $[\bar{1}10]_{CoFe}$ direction

in Fig. 4a, two MgO crystal domains are connected. The right domain has a cube-on-cube orientation with the bottom CoFe, as clearly demonstrated in the NBED pattern in Fig. 4b. The stacking sequence across the interface is …$ABCA_1B_1C_1$..., which is the same as the case described in Fig. 3. The left one, however, has altered its related stacking sequence across the interface to …$ABCB_1A_1C_1$.... The atomic arrangements in this MgO domain and the bottom CoFe appear to be mirror-related to each other with respect to the C plane of CoFe(111), which is apparently different from that of the domain on the right. The twin-like orientation between CoFe and MgO is also clearly revealed by the NBED pattern in Fig. 4c where (111) acts as the twin-like plane. The epitaxial OR between the Type-2 domain of MgO and bottom CoFe is identified as CoFe(111)[$\bar{1}$10] // MgO(111)[1$\bar{1}$0]. Between the two different MgO domains lies a coincidence site lattice (CSL) grain boundary (GB) of Σ3{112}. The repeated structural unit along the domain boundary is outlined by orange-dashed lines (Fig. 4a). Σ3{112} CSL GB has been frequently detected in fcc metals or alloys, and its formation is attributed to the formation of nanotwins during the deformation [55]. In this work, the formation process of the Σ3{112} CSL domain boundary is related to the stacking path of (111) planes during deposition, as depicted in the schematic diagram in Fig. 4d. After the deposition of the C atomic plane of CoFe, a Type-1 domain will be generated when the nearest MgO(111) plane occupies the position of an A_1 plane; simultaneously, a Type-2 domain is formed when the neighboring MgO(111) plane occupies the position of a B_1 plane. The lattice matching details of these two orientations are all consistent with the experimental result in Fig. 4a. Therefore, it is the stacking path of the atomic planes that leads to the formation of the domain boundary. It seems that the Type-1 and Type-2 crystal domains are crystallographically equivalent to each other, and therefore the Type-2 domain could be considered as a variant of the Type-1 crystal domain.

Figure 5 shows the Type-3 domain structure at the CoFe/MgO interface. The atomic ADF-STEM image in Fig. 5a displays another two MgO crystal domains that connect with each other. Clearly, the right side of this image belongs to Type-1 domain, according to the atomic arrangements at the interface and the corresponding NBED pattern in Fig. 5c. Interestingly, its left neighbor has a completely different atomic configuration from the right one, as unambiguously shown in the enlarged image of Fig. 5b. Its corresponding NBED pattern is displayed in Fig. 5d and could not be indexed according to the incident electron beam direction of MgO<$\bar{1}$10>. Close examination reveals that the NBED pattern can be well indexed according to the MgO[11$\bar{2}$] direction. Therefore, this novel epitaxial orientation between the Type-3 domain and the bottom CoFe is expressed as CoFe(111)[$\bar{1}$10] // MgO(111)[11$\bar{2}$]. The extension of the {111} atomic planes from Type-1 domain (right) to Type-3 domain (left) is also observed in Fig. 5a, indicating the formation of a coherent boundary between them. Careful inspection suggests that the interface boundary has a zigzag morphology, with two types of linear facets of $(\bar{1}\bar{1}1)_{\text{Type-1}}/(5\bar{3}1)_{\text{Type-3}}$ and $(111)_{\text{Type-1}}/(111)_{\text{Type-3}}$ (Fig. R1). Here, to verify the occurrence of Type-3 domain in the MgO layer, we observed the sample from another direction that deviates CoFe[$\bar{1}$10] by 30° within the film plane, with the corresponding image shown in Fig. 5e. This atomic ADF-STEM image is recorded with the incident electron beam parallel to the CoFe[11$\bar{2}$] direction, as indicated by the atomic-resolution images of CoFe in the lower-right inset. Within the MgO barrier, the viewing direction is parallel to MgO<$\bar{1}$10> and the stacking sequence of $A_1B_1C_1A_1B_1C_1$ is again revealed, which is in good agreement with the proposed epitaxial orientation of Type-3. Figures 5f and 5g illustrate the atomic lattice matching between the Type-3 MgO crystal domain and CoFe along the viewing direction of CoFe[$\bar{1}$10] and CoFe[11$\bar{2}$], respectively. As indicated by the traces of atomic planes of CoFe(11$\bar{1}$) and MgO(2$\bar{2}$0) marked by yellow and orange lines in Figs. 5b and 5f, the two lattices are well matched along the horizontal direction, with

only a rather small elastic strain of 3.4% at the interface. A similar strain value could also be computed according to the atomic configuration in Fig. 5g, where the interface is viewed along the CoFe[11$\bar{2}$] direction.

Apart from the combined structure where one MgO domain contacts with another as shown in Figs. 4 and 5, several domains can also coexist even in a very small region. The ADF-STEM in Fig. 6 displays a representative atomic configuration of the multiple nano-domains in the MgO barrier. According to this image, the bottom CoFe layer is atomically flat. However, after the MgO barrier deposition on the CoFe surface, four MgO crystal domains with different configurations are formed, with an average domain size of ~4 nm. The enlarged images of these four domains reveal that in this small local region, 3 types of crystal domains can coexist in the MgO barrier. A statistical analysis implies that the relative number density of the Type-1, Type-2 and Type-3 domains are 42/98, 30/98 and 26/98, respectively, among the 98 crystal domains counted in the present work. The fraction of Type-1 crystal domain is ~1.5 times higher than that of Type-3 domain. Close examination of the atomic arrangements in the MgO barrier indicates that the traces of MgO{111} planes have extended through all the crystal domains inside, which can well explain the formation of the preferential (111) orientation (texture) in the MgO layer. Due to the occurrence of a large number of MgO crystal domains in the barrier, the growth quality of the upper CoFe layer appears to be significantly degraded, far inferior to that of the bottom CoFe. Besides, it is to be noted that the observation of 3 different types of ORs in the fcc(111)-oriented MTJ would provide a degree of freedom to choose the epitaxial growth mode between fcc-structured FM and barrier layers, if the formation of these 3 types of nano domains is selectively controlled. This is in sharp contrast to the case of conventional bcc-(001) MTJs (with only 1 epitaxial growth mode).

4. Discussion

4.1. Formation mechanism of different MgO domains

In this study, abundant MgO nano-crystal domains have been detected in the MgO barrier of the MTJ and their configurations can be categorized into three kinds, including Type-1, Type-2, and Type-3 (Figs. 3-5). The corresponding OR between rocksalt MgO domains and fcc-CoFe is expressed as follows: CoFe(111)[$\bar{1}$10] // MgO(111)[$\bar{1}$10] (Type-1 OR), CoFe(111)[$\bar{1}$10] // MgO(111)[1$\bar{1}$0] (Type-2 OR), and CoFe(111)[$\bar{1}$10] // MgO(111)[11$\bar{2}$] (Type-3 OR). Two or more MgO crystal domains can even coexist at a highly localized region in the MgO layer (Figs. 4-6). Meanwhile, (111) atomic planes have been observed to extend through several adjacent domains (Figs. 4-6), which leads to a fully epitaxial growth of the (111) orientation in the MTJ from the bottom to top electrodes. The observation of the atomically flat surface of the bottom CoFe (Fig. 6) suggests that during deposition three types of domains are likely to nucleate concurrently on the surface of the CoFe electrode, which also agrees with the relatively large volume fraction of each type. A comparison of the film growth quality between the top and bottom CoFe layers (Fig. 6) indicates that the formation of plentiful MgO nano domains in the barrier, to some extent, could also affect the growth of the subsequent layer.

The formation mechanism of the different MgO domains in the barrier is discussed below in terms of atomic matching at the CoFe/MgO interface as shown in Fig. 7. Schematic diagrams of the rocksalt MgO and fcc-CoFe crystal lattices are shown in Figs. 7a and 7b, respectively. These two types of lattices have the same space group of Fm$\bar{3}$m, and their structures are almost the same if the

O atoms in MgO are neglected. For simplicity, only Mg atoms are shown for the MgO lattice. Figures 7c and 7e depict the in-plane lattice matching between CoFe(111) and MgO(111) atomic planes, corresponding to Type-1 (cube-on-cube) and Type-3 ORs, respectively. The near-coincidence sites (NCSs) are outlined by black dashed circles. In general, the higher the number density of NCSs between two atomic planes, the lower energy for this kind of lattice matching. In the Type-1 lattice match between CoFe(111) and MgO(111), CoFe[$\bar{1}$10] is parallel to MgO[$\bar{1}$10]. The mismatch along this direction is calculated to be (5.95 – 4.98) / 4.98 × 100% = +19.6%. To accommodate such a large strain at the interface, periodic misfit dislocations are inevitably formed, as confirmed in Fig. 3e. Such a large interfacial strain also indicates the daunting challenge of the single-crystalline epitaxial growth in the MgO(111) barrier. Figure 7d displays the projected atomic arrangements along the [111] direction. There are three different {111} atomic planes along the projection direction of [111], represented by A, B and C, respectively. Assuming that the uppermost layer of CoFe is a C layer, atoms from MgO will have two options during deposition: either taking the atomic sites of the A or B layer. If the A layer is occupied above the CoFe surface, the stacking sequence at the interface will be …$ABCA_1B_1C_1$... (Fig. 4), leading to the Type-1 atomic matching at the CoFe/MgO interface; but if the B layer is occupied, the stacking sequence will change to …$ABCA_1B_1C_1$..., and the twin-like orientation (i.e., Type-2 OR) will be successfully formed (Fig. 4). Therefore, the Type-2 lattice matching is essentially similar to the Type-1 lattice matching and can be considered as a variant of the latter. In addition, crystallographic analysis suggests that Type-3 OR will be readily obtained if a 30° in-plane rotation of the MgO lattice is introduced to the case of the Type-1 lattice matching, as clearly shown in Fig. 7e. In the direction of [1$\bar{1}$0] // [2$\bar{1}\bar{1}$], the lattice mismatch is calculated as (5.15 – 4.98) / 4.98 × 100% = +3.4%. It has been reported that the structural stability of an interface is determined by the interfacial energy, i.e., the interface stability increases with the decreasing interfacial energy [56, 57]. Type-3 CoFe/MgO interface should have a slightly higher interfacial energy than Type-1 CoFe/MgO interface since the volume fraction of Type-1 crystal domain is 1.5 times higher than that of Type-3 domain according to the statistic analysis.

4.2. Impacts of MgO domains on a TMR ratio (DFT calculations)

We next discuss and compare the impacts of different types of MgO crystal domains on the TMR ratio of the CoFe/MgO/CoFe (111)-oriented MTJ. In a recent theoretical study, Masuda *et al.* [37] reported a large TMR ratio over 2000% in the fcc-Co/MgO/Co(111) junction with a Type-1 (cube-on-cube) OR at the Co/MgO interface, where the large ratio originates from the interfacial resonance effect rather than the coherent tunneling mechanism of bulk Λ_1 states in the barrier and electrodes of Co/STO/Co(111) and Ni/STO/Ni(111) MTJs [58]. In their calculation, the Co lattice parameter in the supercell was fixed to the bulk value of 0.28 nm fixed but the MgO lattice parameter deviated from the bulk value due to the presumed strain relaxation at the interface, leading to the change of the MgO crystal structure from the rocksalt type to orthogonal type (in-plane compressed and out-of-plane elongated) and thus the formation of the misfit dislocation-free Co/MgO interfaces. However, in the actual experimental results with a MgO barrier thickness of ~3 nm (Fig. 3), MgO still adopts a rocksalt crystal structure with a lattice parameter a = 0.420 nm, and periodic misfit dislocations always occur at the Co/MgO interface. Such a large interfacial strain (~19.6%) seems to be rather difficult to relax elastically at the interface, and therefore must be mediated by the formation of periodic interfacial misfit dislocations (Fig. 3e). Previous reports have shown that interfacial misfit dislocations are detrimental to TMR [59, 60]. In our study, the high number density of interfacial misfit dislocations

at the CoFe/MgO interface with a Type-1 OR would cause undesirable electron scattering and lower the TMR ratio of the local region with Type-1. Due to the relative high proportion (about 40%) of Type-1 MgO domain in the film, it seems reasonable to conclude that the high number density of interfacial dislocations at Type-1 CoFe/MgO interfaces is a possible reason for the much smaller experimental TMR ratio (~37%) than the theoretical value of over 2000% calculated for the (111) MTJ with a fully Type-1 OR.

As mentioned earlier, the Type-2 OR is almost similar to the Type-1 OR case from a crystallographic perspective. Therefore, a Type-2 (111) MTJ should have nearly the same value of a TMR ratio as the Type-1 (111) MTJ, and both should share the same tunneling mechanism. The Type-3 MgO domain is structurally different from the Type-1 and Type-2 domains and has a volume fraction of ~1/4 in the MgO barrier layer, which has never been reported experimentally or theoretically in previous studies. It is reasonable to speculate that the Type-3 domains should also affect the TMR ratio in our study. To quantify the possible influence of the Type-3 MgO domain on the TMR ratio, first-principles calculations were performed here to systematically investigate the corresponding tunneling process for the Type-3 OR MTJ.

Figure 8 shows the supercell structure of the Type-3 OR Co/MgO/Co(111) MTJ. The MgO barrier thickness is ~1.07 nm, same as the value in a previous study [37], and for simplicity, pure Co is used as the ferromagnetic layer in the MTJ. The Type-3 OR is clearly displayed in the [111]-projected atomic model in Fig. 8b. The calculation result in Fig. 9 shows the $\mathbf{k}_{\|}$ dependences of conductances of the Type-3 (111) MTJ. Results for $\mathbf{k}_{\|}$-resolved majority-spin conductance $G_{P,\uparrow}(\mathbf{k}_{\|})$ and minority-spin conductance $G_{P,\downarrow}(\mathbf{k}_{\|})$ in the P states are shown in Figs. 9a and 9b, respectively, and the result for majority-spin conductance $G_{AP,\uparrow}(\mathbf{k}_{\|})$ in the AP states shown in Fig. 9c. It is clearly shown that the maximum tunneling conductances of $G_{P,\uparrow}(\mathbf{k}_{\|})$, $G_{P,\downarrow}(\mathbf{k}_{\|})$ and $G_{AP,\uparrow}(\mathbf{k}_{\|})$ in Fig. 9 do not locate at the Γ point $\mathbf{k}_{\|} = \mathbf{0}$ but around the Γ point, leading to a ring-like distribution of the conductances, which resembles the case of cube-on-cube (i.e., Type-1) Co/MgO/Co(111) [37] and $L1_1$-CoPt/MgO/$L1_1$-CoPt(111) MTJ [50], but significantly differentiates from the case of Fe(Co)/MgO/Fe(Co)(001) junction where the maximum conductance lies in the Γ center and the bulk majority-spin Δ_1 state dominates the transmission probability [1, 2]. In addition, the conductance values of $G_{P,\uparrow}(\mathbf{k}_{\|})$ and $G_{AP,\uparrow}(\mathbf{k}_{\|})$ distribute more widely than that of $G_{P,\downarrow}(\mathbf{k}_{\|})$, and $G_{P,\downarrow}(\mathbf{k}_{\|})$ is ~3 times of magnitude higher than that of $G_{P,\uparrow}(\mathbf{k}_{\|})$ and $G_{AP,\uparrow}(\mathbf{k}_{\|})$.

Table 1 lists the calculated total conductances and theoretical TMR ratios of Type-3 and Type-1 Co/MgO/Co(111) MTJs in the P and AP states. It shows that the minority-spin channel $G_{P,\downarrow}$ dominates the coherent tunneling process, which is in sharp contrast to the cube-on-cube oriented (111) MTJ cases [37, 50]. However, the total parallel conductance G_P and antiparallel conductance G_{AP} in the Type-3 Co/MgO/Co(111) MTJ exhibit only a slight difference, yielding a rather small calculated TMR ratio of ~17%. These results are further compared with those obtained in the Type-1 Co/MgO/Co(111) MTJ, as shown in Table 1. In the Type-1 Co/MgO/Co(111) MTJ case, however, the conductance of $G_{P,\uparrow}$ has the largest value and the P conductance G_P is more than 20 times of magnitude higher than G_{AP}, which leads to a TMR ratio over 2000% [37]. Clearly, the TMR ratio of the Type-3 (111) MTJ is much smaller than that of the Type-1 (111) MTJs, with a difference of two orders of magnitude.

The spin-dependent electron tunneling process of the Type-3 (111)-oriented MTJ is also investigated and discussed. It is to be noted that in the Fe/MgO/Fe(001)-oriented MTJ electron tunneling mainly occurs at Γ point $\mathbf{k}_{\|} = \mathbf{0}$ [1], but in the Type-1 (111)-oriented MTJ, the $\mathbf{k}_{\|}$-resolved tunneling probability reaches the maximum value around the Γ point [37]. The tunneling mechanism

of the former is related to coherent tunneling of bulk Δ_1 states and that of the latter, instead, is considered to result from the interfacial resonance effect, where antibonding is formed between interfacial Co *d*-orbitals and O *p*-orbitals [37, 50]. In the present work, the distribution pattern of the conductance of the Type-3 (111)-oriented MTJ is similar to that of the Type-1 (111) MTJ, which indicates that a similar mechanism of interfacial resonance tunneling should also operate in the Type-3 (111)-oriented MTJ. Therefore, to verify such a tunneling mechanism in the Type-3 Co/MgO/Co (111) MTJ, here we performed the local density of state (LDOS) analysis of the interfacial Co atoms in the Co/MgO interface, by following the approach of our previous studies [37, 50]. The corresponding result is shown in Fig. 10. Four interfacial Co atoms at the interface in Fig. 10a are selected, denoted by Co13, Co14, Co15 and Co16, respectively, and the calculation results for these four Co atoms are quite similar. Therefore, for simplicity, only the result for Co15 is shown in Figs. 10b and 10c. The corresponding LDOS profiles of the interfacial Co atom in Fig. 10b reveal that at the Fermi energy level, large LDOS lies in the minority-spin channels (↓) where the d_{yz} and d_{xy} minority-spin states contribute most. Figure 10c further shows the $\mathbf{k}_{\|}$-resolved LDOSs of the interfacial Co *d*-orbital majority- and minority-spin states at the Fermi level. Clearly, the distribution of $\mathbf{k}_{\|}$ points with large LDOS (i.e., minority-spin states) has a ring-like shape, which is quite similar to the ring-like distribution pattern of $G_{P,\downarrow}(\mathbf{k}_{\|})$ with large conductance (Fig. 9b). This also indicates that the interfacial Co states play a dominant role in the TMR effect in the Type-3 (111)-oriented MTJ.

In the present study, three types ORs were found in our MTJ and the experimental TMR ratio was 36.8%, which is larger than the calculated TMR ratio of the Type-3 MTJ (17%), but much smaller than that of the Type-1 MTJ (over 2000%). According to the calculation results shown in Table 1, the Type-3 domains in the barrier would have a lower resistance than that of the Type-1 domains for the AP state, while they would have a higher resistance than that of the Type-1 domains for the P state. This indicates that most of the injected charge currents would preferentially flow into the Type-1 domains in the P state, but into the Type-3 domains in the AP state, which will definitely yield a smaller TMR ratio in the experiment.

4.3. Implications for the design of future (111)-oriented MTJs

A discrepancy of several orders of magnitude has been reported between the experimental and theoretical TMR ratios in the Co(Fe)/MgO/Co(Fe) (001)-oriented MTJs. According to previous studies, the origin of the large discrepancy in (001)-oriented MTJs is supposed to be mainly associated with rough interfaces, poor barrier crystallinity, O vacancies at the Co(Fe)/MgO interface, and large interfacial strains due to lattice mismatch [5, 15, 17]. Therefore, a better-controlled film preparation, such as the degree of oxidation of the barrier and crystallinity of different layers, is the key to enhance the TMR ratio in MTJs. For example, Scheike *et al.* [9] recently carefully optimized the growth conditions for each layer and successfully achieved high-quality epitaxial growth and chemically sharp interfaces, which doubled the TMR ratio to be 417% at RT in the typical Fe/MgO/Fe(001) MTJ. However, many interfacial dislocations still existed due to the lattice mismatch of 3.8% between Fe and MgO. To lower the number density of such interfacial dislocations, a Mg_4Al-Ox barrier was used to reduce the lattice mismatch [17]. Therefore, the TMR ratio is further enhanced to 429% at RT and 1034% at 10 K in a Fe/Mg_4Al-Ox/Fe(001) MTJ [60]. Here, similar strategies could also be applied to rationally design future high-quality (111)-oriented MTJs.

Firstly, misfit strain at the interface of an fcc-structured FM(111)/barrier(111) should be minimal

to maximize the interfacial resonant tunneling. The crystallographic analysis shown in Fig. 11 provides a crystallographic perspective on the misfit strains at the FM/barrier interface. Figures 11a1 and 11b1 display the atomic arrangements of the Type-1 (or Type-2) and the Type-3 lattice matching between $Co_{90}Fe_{10}$(111) and MgO(111) planes, respectively. The mismatch at the interface is +19.6% for the former and +3.4% for the latter. As revealed by the observation in Fig. 3, the large interfacial strain of 19.6% is too hard to be elastically relaxed at the interface, and consequently, must be accommodated by periodic interfacial misfit dislocations. Similar to the case of Al-doping into MgO to tune the barrier lattice parameter [8, 16, 60-62], atomic doping could also be used to shrink the lattice parameter of the barrier to achieve a perfect lattice matching, i.e., leading to the formation of crystallographically coherent and dislocation-free barrier/electrode interfaces (Fig. 11a2). Simultaneously, the misfit stain in the Type-3 lattice matching would be altered from 3.4% to –13.4% (Fig. 11a3), which means that the Type-1 (Type-2) epitaxial growth becomes favorable and dominant, while the Type-3 epitaxial growth is substantially suppressed from an elastic strain energy point of view. However, epitaxial growth of the Type-3 orientation can be preferentially achieved when atomic doping increases the lattice parameter of FM from a = 0.352 nm to 0.364 nm, so that lattice optimization achieves the perfect Type-3 lattice matching (Fig. 11b2), while the Type-1 and Type-2 orientations between the fcc-FM and barrier would both be unfavorable to form due to a huge misfit strain at the interface (+16.1%, Fig. 11b3). Atomic doping into the lattice could alter the corresponding lattice constants, thereby enabling to precisely control interfacial misfit strain and providing a degree of freedom to selectively choose the desired epitaxial growth mode between fcc-structured FM/barrier layers. In addition, atomic doping is also an effective method to modify the electronic structure of barrier and electrode layers, which can tune the TMR effect [8, 19, 63]. As indicated by the theoretical results in Table 1, the calculated TMR ratio in the Type-1 Co/MgO/MgO (111) is two orders of magnitude larger than that in the Type-3 one. Such a substantial discrepancy suggests that the future design of a Co-based (111) MTJ should adopt and focus on the Type-1 (111)-orientation. Therefore, a perfect lattice matching might be achieved in the Co-based (111) MTJ when over-sized atoms such as Pt and Pd are doped into the Co electrode, and under-sized Al is doped into the MgO barrier. In addition, CoPt(111) and CoPd(111) alloys exhibit a large PMA energy beyond 1 MJ/m^3 [25, 27, 33]. Therefore, the atomic doping of Pt or Pd in the Co-based (111)-oriented MTJ is expected not only to significantly improve the TMR ratio, but also to achieve a large PMA, which is of great significance for the design of ultra-high-density MRAM cells below a 10 nm scale.

In addition, well-controlled oxidation of the barrier interface is required. For example, it has been theoretically and experimentally demonstrated that O vacancies (oxygen-poor condition) significantly decrease the TMR ratio due to the undesirable non-resonant tunneling in (001)-oriented MTJs [4, 7, 18, 64]. Such phenomena would also be expected in the (111)-oriented MTJs, indicating the necessity of lowering O vacancy concentration in the barrier interface to obtain a large TMR. Over-oxidation of the barrier also remarkably reduces the TMR ratio due to suppression of the effective spin polarization of the FMs [65, 66]. Such an over-oxidation effect is clearly observed in a thin MgO barrier region (~2 nm), as shown in Fig. 12. We found that this sample has a negligibly small TMR ratio, although the good epitaxial growth with (111) orientation and relatively flat barrier interfaces are confirmed by Fig. 12a. The corresponding EDS mapping analysis shows that the O thickness is slightly wider than the Mg thickness, and the O signal extends beyond the CoFe/MgO interface boundary as marked by the dashed yellow lines, which is different from the observation of the 3-nm-thick MgO barrier sample (Fig. 2). This indicates that O has diffused into the CoFe electrode and oxidized the adjacent electrode due to our deposition process. Furthermore, the Fe EDS map in

Fig. 12 b and the Fe line profile in Fig. 12c clearly show that Fe atoms have segregated to the CoFe/MgO interface (see the arrows in Fig. 12c). The O elemental distribution pattern and Fe segregation at the interface can be attributed to the stronger chemical affinity between Fe and O than that between Co and O. Therefore, a careful and precise control of the degree of oxidation in the barrier interface is of great importance to obtain a large TMR ratio in (111)-MTJs.

5. Conclusions and outlook

In this study, the TMR effect of the novel fully epitaxial CoFe/MgO/CoFe fcc(111)-oriented MTJ has been systematically investigated via microstructure analyses and first-principles calculations. The main conclusions are summarized as follows:

1. Nano-crystal domain structures are frequently observed in the MgO(111) barrier layer, yielding three types of ORs between the CoFe and MgO layers in the (111)-textured CoFe/MgO/CoFe MTJ, including cube-on-cube type (Type-1), twin-like type (Type-2) and an unexpected type (Type-3). The volume fraction of Type-1, Type-2 and Type-3 MgO domains are 42/98, 30/98 and 26/98, respectively. The (111) textured MgO barrier is formed by the extension of {111} atomic planes through multiple adjacent MgO domains, which leads to the fully (111) epitaxial growth in the MTJ from the bottom to top electrodes. Meanwhile, the formation of multiple MgO domains significantly affects the growth quality of the subsequent top CoFe.
2. The corresponding three ORs between rocksalt MgO domains and fcc CoFe are found: CoFe(111)[$\bar{1}$10] // MgO(111)[$\bar{1}$10] (Type-1 OR), CoFe(111)[$\bar{1}$10] // MgO(111)[1$\bar{1}$0] (Type-2 OR), and CoFe(111)[$\bar{1}$10] // MgO(111)[11$\bar{2}$] (Type-3 OR). Crystallographic analysis suggests that the Type-2 OR is a variant of the Type-1 OR resulting from the different stacking orders of MgO(111) atomic planes during the deposition process, while the Type-3 OR is easily formed when the MgO lattice is rotated in-plane by 30° relative to the Type-1 OR. The in-plane lattice mismatch between Co(111) and MgO(111) is 19.6% for the Type-1 and Type-2 ORs, and 3.4% for the Type-3 OR.
3. First-principles calculations are performed to quantitatively investigate the impact of MgO crystal domains on the TMR ratio of the MTJ. The theoretical TMR ratio of the Co/MgO/Co(111) MTJ with the Type-3 OR is only 17%, two orders of magnitude smaller than that with the Type-1 or Type-2 OR, which will provide another reasonable explanation for the small experimental TMR ratio. In addition, the tunneling mechanism in the Type-3 OR is dominated by the interfacial resonant effect, which is similar to the Type-1 OR but different from the (001)-oriented MTJs where the coherent tunneling mechanism of the bulk Δ_1 bands dominates.

Conventional bcc-(001) MTJs have only 1 epitaxial growth mode, but there are 3 types of epitaxial growth modes in the present fcc(111) MTJs. The “nano-domain degree of freedom” of the fcc(111) MTJs is expected to expand the variety of spintronic heterostructure designs. For example, atomic doping of oversized atoms such as Pt and Pd into the Co electrode, and undersized Al atoms into the MgO barrier could be applied to optimize lattice constants in the Type-1 OR to reduce electronic diffuse scattering due to a better lattice matching, while suppressing the formation of the Type-3 OR.

Acknowledgments

This research was partly supported by JST CREST (JPMJCR19J4), and JSPS KAKENHI Grant

Nos. 20K14782, 21H01750, 22H04966, and 23K03933. C. He wishes to acknowledge the access to electron microscopies in Research Center for Magnetic and Spintronic Materials in NIMS and gratefully thank Mr J. Uzuhashi and Mrs K. Suzuki for their suggesions on TEM sample preparation by focus ion beam. J.Y. Song would like to acknowledge NIMS for the provision of a NIMS Junior Research Assistantship.

Competing interests

The authors declare no competing interests.

References

[1] W.H. Butler, X.G. Zhang, T.C. Schulthess, J.M. MacLaren, Spin-dependent tunneling conductance of Fe/MgO/Fe sandwiches, Phys. Rev. B 63 (2001) 054416.

[2] J. Mathon, A. Umerski, Theory of tunneling magnetoresistance of an epitaxial Fe/MgO/Fe(001) junction, Phys. Rev. B 63 (2001) 220403.

[3] S.S.P. Parkin, C. Kaiser, A. Panchula, P.M. Rice, B. Hughes, M. Samant, S.-H. Yang, Giant tunnelling magnetoresistance at room temperature with MgO (100) tunnel barriers, Nat. Mater. 3 (2004) 862-867.

[4] S. Yuasa, T. Nagahama, A. Fukushima, Y. Suzuki, K. Ando, Giant room-temperature magnetoresistance in single-crystal Fe/MgO/Fe magnetic tunnel junctions, Nat. Mater. 3 (2004) 868-871.

[5] C. Heiliger, P. Zahn, B.Y. Yavorsky, I. Mertig, Interface structure and bias dependence of Fe/MgO/Fe tunnel junctions: Ab initio calculations, Phys. Rev. B 73 (2006) 214441.

[6] S. Yuasa, D.D. Djayaprawira, Giant tunnel magnetoresistance in magnetic tunnel junctions with a crystalline MgO(001) barrier, J. Phys. D: Appl. Phys 40 (2007) R337-R354.

[7] Y. Ke, K. Xia, H. Guo, Oxygen-vacancy-induced diffusive scattering in Fe/MgO/Fe magnetic tunnel junctions, Phys. Rev. Lett. 105 (2010) 236801.

[8] H. Sukegawa, Y. Miura, S. Muramoto, S. Mitani, T. Niizeki, T. Ohkubo, K. Abe, M. Shirai, K. Inomata, K. Hono, Enhanced tunnel magnetoresistance in a spinel oxide barrier with cation-site disorder, Phys. Rev. B 86 (2012) 184401.

[9] T. Scheike, Q. Xiang, Z. Wen, H. Sukegawa, T. Ohkubo, K. Hono, S. Mitani, Exceeding 400% tunnel magnetoresistance at room temperature in epitaxial Fe/MgO/Fe(001) spin-valve-type magnetic tunnel junctions, Appl. Phys. Lett. 118 (2021) 042411.

[10] X.G. Zhang, W.H. Butler, Large magnetoresistance in bcc Co/MgO/Co and FeCo/MgO/FeCo tunnel junctions, Phys. Rev. B 70 (2004) 172407.

[11] S. Yuasa, A. Fukushima, H. Kubota, Y. Suzuki, K. Ando, Giant tunneling magnetoresistance up to 410% at room temperature in fully epitaxial Co/MgO/Co magnetic tunnel junctions with bcc Co(001) electrodes, Appl. Phys. Lett. 89 (2006) 042505.

[12] Y.M. Lee, J. Hayakawa, S. Ikeda, F. Matsukura, H. Ohno, Effect of electrode composition on the tunnel magnetoresistance of pseudo-spin-valve magnetic tunnel junction with a MgO tunnel barrier, Appl. Phys. Lett. 90 (2007) 212507.

[13] S. Ikeda, J. Hayakawa, Y. Ashizawa, Y.M. Lee, K. Miura, H. Hasegawa, M. Tsunoda, F. Matsukura, H. Ohno, Tunnel magnetoresistance of 604% at 300K by suppression of Ta

diffusion in CoFeB/MgO/CoFeB pseudo-spin-valves annealed at high temperature, Appl. Phys. Lett. 93 (2008) 082508.
[14] X.D. Xu, K. Mukaiyama, S. Kasai, T. Ohkubo, K. Hono, Impact of boron diffusion at MgO grain boundaries on magneto-transport properties of MgO/CoFeB/W magnetic tunnel junctions, Acta Mater. 161 (2018) 360-366.
[15] T. Scheike, Z. Wen, H. Sukegawa, S. Mitani, 631% room temperature tunnel magnetoresistance with large oscillation effect in CoFe/MgO/CoFe(001) junctions, Appl. Phys. Lett. 122 (2023) 112404.
[16] H. Sukegawa, H. Xiu, T. Ohkubo, T. Furubayashi, T. Niizeki, W. Wang, S. Kasai, S. Mitani, K. Inomata, K. Hono, Tunnel magnetoresistance with improved bias voltage dependence in lattice-matched Fe/spinel $MgAl_2O_4$/Fe(001) junctions, Appl. Phys. Lett. 96 (2010) 212505.
[17] J.P. Hadorn, H. Sukegawa, T. Ohkubo, S. Mitani, K. Hono, Microstructural evolution of perpendicular magnetization films with an ultra-thin $Co_2FeAl/MgAl_2O_4$(001) structure, Acta Mater. 145 (2018) 306-315.
[18] J.P. Velev, K.D. Belashchenko, S.S. Jaswal, E.Y. Tsymbal, Effect of oxygen vacancies on spin-dependent tunneling in Fe/MgO/Fe magnetic tunnel junctions, Appl. Phys. Lett. 90 (2007) 072502.
[19] A.P. Chen, J.D. Burton, E.Y. Tsymbal, Y.P. Feng, J. Chen, Effects of B and C doping on tunneling magnetoresistance in CoFe/MgO magnetic tunnel junctions, Phys. Rev. B 98 (2018) 045129.
[20] T. Yamamoto, T. Nozaki, K. Yakushiji, S. Tamaru, H. Kubota, A. Fukushima, S. Yuasa, Perpendicular magnetic anisotropy and its voltage control in MgO/CoFeB/MgO junctions with atomically thin Ta adhesion layers, Acta Mater. 216 (2021) 117097.
[21] K. Yakushiji, T. Saruya, H. Kubota, A. Fukushima, T. Nagahama, S. Yuasa, K. Ando, Ultrathin Co/Pt and Co/Pd superlattice films for MgO-based perpendicular magnetic tunnel junctions, Appl. Phys. Lett. 97 (2010) 232508.
[22] S. Ikeda, K. Miura, H. Yamamoto, K. Mizunuma, H.D. Gan, M. Endo, S. Kanai, J. Hayakawa, F. Matsukura, H. Ohno, A perpendicular-anisotropy CoFeB–MgO magnetic tunnel junction, Nat. Mater. 9 (2010) 721-724.
[23] S.H. Kang, K. Lee, Emerging materials and devices in spintronic integrated circuits for energy-smart mobile computing and connectivity, Acta Mater. 61 (2013) 952-973.
[24] G.-G. An, J.-B. Lee, S.-M. Yang, J.-H. Kim, W.-S. Chung, J.-P. Hong, Highly stable perpendicular magnetic anisotropies of CoFeB/MgO frames employing W buffer and capping layers, Acta Mater. 87 (2015) 259-265.
[25] P.F. Carcia, Perpendicular magnetic anisotropy in Pd/Co and Pt/Co thin-film layered structures, J. Appl. Phys. 63 (1988) 5066-5073.
[26] S. Mangin, D. Ravelosona, J.A. Katine, M.J. Carey, B.D. Terris, E.E. Fullerton, Current-induced magnetization reversal in nanopillars with perpendicular anisotropy, Nat. Mater. 5 (2006) 210-215.
[27] J.-H. Park, C. Park, T. Jeong, M.T. Moneck, N.T. Nufer, J.-G. Zhu, Co/Pt multilayer based magnetic tunnel junctions using perpendicular magnetic anisotropy, J. Appl. Phys. 103 (2008) 07A917.
[28] K. Yakushiji, K. Noma, T. Saruya, H. Kubota, A. Fukushima, T. Nagahama, S. Yuasa, K. Ando, High magnetoresistance ratio and low resistance–area product in magnetic tunnel junctions with perpendicularly magnetized electrodes, Appl. Phys. Express 3 (2010) 053003.

[29] B. Jinnai, C. Zhang, A. Kurenkov, M. Bersweiler, H. Sato, S. Fukami, H. Ohno, Spin-orbit torque induced magnetization switching in Co/Pt multilayers, Appl. Phys. Lett. 111 (2017) 102402.
[30] M. Wang, W. Cai, K. Cao, J. Zhou, J. Wrona, S. Peng, H. Yang, J. Wei, W. Kang, Y. Zhang, J. Langer, B. Ocker, A. Fert, W. Zhao, Current-induced magnetization switching in atom-thick tungsten engineered perpendicular magnetic tunnel junctions with large tunnel magnetoresistance, Nat. Commun. 9 (2018) 671.
[31] B. Jinnai, H. Sato, S. Fukami, H. Ohno, Scalability and wide temperature range operation of spin-orbit torque switching devices using Co/Pt multilayer nanowires, Appl. Phys. Lett. 113 (2018) 212403.
[32] H. Meng, J.-P. Wang, Spin transfer in nanomagnetic devices with perpendicular anisotropy, Appl. Phys. Lett. 88 (2006) 172506.
[33] J. Lee, G. An, S. Yang, W. Chung, J. Hong, Thermally stable perpendicular magnetic anisotropy features of $[Co/Pd]_m$ multilayer matrix integrated with $[CoO/Pd]_n$ bottom layer, Appl. Phys. Lett. 104 (2014) 022404.
[34] K. Mizunuma, S. Ikeda, J.H. Park, H. Yamamoto, H. Gan, K. Miura, H. Hasegawa, J. Hayakawa, F. Matsukura, H. Ohno, MgO barrier-perpendicular magnetic tunnel junctions with CoFe/Pd multilayers and ferromagnetic insertion layers, Appl. Phys. Lett. 95 (2009) 232516.
[35] K. Mizunuma, M. Yamanouchi, S. Ikeda, H. Sato, H. Yamamoto, H.-D. Gan, K. Miura, J. Hayakawa, F. Matsukura, H. Ohno, Pd Layer Thickness Dependence of Tunnel Magnetoresistance Properties in CoFeB/MgO-Based magnetic tunnel junctions with perpendicular anisotropy CoFe/Pd multilayers, Appl. Phys. Express 4 (2011) 023002.
[36] M. Ohtake, D. Suzuki, M. Futamoto, F. Kirino, N. Inaba, Preparation of $L1_1$-CoPt/MgO/$L1_1$-CoPt tri-layer film on Ru(0001) underlayer, AIP Adv. 6 (2016) 056103.
[37] K. Masuda, H. Itoh, Y. Miura, Interface-driven giant tunnel magnetoresistance in (111)-oriented junctions, Phys. Rev. B 101 (2020) 144404.
[38] M. Ohtake, O. Yabuhara, Y. Nukaga, M. Futamoto, Preparation of Co (0001) hcp and (111) fcc films on single-crystal oxide substrates, J. Phys. Conf. Ser., IOP Publishing, 2011, p. 012016.
[39] A.-C. Sun, F.-T. Yuan, J.-H. Hsu, H.Y. Lee, Evolution of structure and magnetic properties of sputter-deposited CoPt thin films on MgO(111) substrates: Formation of the $L1_1$ phase, Scr. Mater. 61 (2009) 713-716.
[40] J.Y. Song, T. Scheike, C. He, Z. Wen, T. Ohkubo, K. Hono, H. Sukegawa, S. Mitani, Fully epitaxial fcc(111) magnetic tunnel junctions with a $Co_{90}Fe_{10}$/MgAlO/ $Co_{90}Fe_{10}$ structure, arXiv preprint arXiv: https://doi.org/10.48550/arXiv.2308.04149, (2023).
[41] D. Rafaja, C. Schimpf, V. Klemm, G. Schreiber, I. Bakonyi, L. Péter, Formation of microstructural defects in electrodeposited Co/Cu multilayers, Acta Mater. 57 (2009) 3211-3222.
[42] G. Kresse, J. Furthmüller, Efficient iterative schemes for ab initio total-energy calculations using a plane-wave basis set, Phys. Rev. B 54 (1996) 11169-11186.
[43] J.P. Perdew, K. Burke, M. Ernzerhof, Generalized gradient approximation made simple, Phys. Rev. Lett. 77 (1996) 3865-3868.
[44] G. Kresse, D. Joubert, From ultrasoft pseudopotentials to the projector augmented-wave method, Phys. Rev. B 59 (1999) 1758-1775.
[45] A. Smogunov, A. Dal Corso, E. Tosatti, Ballistic conductance of magnetic Co and Ni nanowires with ultrasoft pseudopotentials, Phys. Rev. B 70 (2004) 045417.

[46] P. Giannozzi, S. Baroni, N. Bonini, M. Calandra, R. Car, C. Cavazzoni, D. Ceresoli, G.L. Chiarotti, M. Cococcioni, I. Dabo, QUANTUM ESPRESSO: a modular and open-source software project for quantum simulations of materials, J. Phys. Condens. Matter 21 (2009) 395502.
[47] P. Giannozzi, O. Andreussi, T. Brumme, O. Bunau, M.B. Nardelli, M. Calandra, R. Car, C. Cavazzoni, D. Ceresoli, M. Cococcioni, Advanced capabilities for materials modelling with Quantum ESPRESSO, J. Phys. Condens. Matter 29 (2017) 465901.
[48] We used the pseudopotentials Co.pbe-n-rrkjus_psl.0.2.3.UPF, Mg.pbe-n-rrkjus_psl.0.3.0.UPF, and O.pbe-nl-rrkjus_psl.1.0.0.UPF from https://www.quantum-espresso.org.
[49] H.J. Choi, J. Ihm, Ab initio pseudopotential method for the calculation of conductance in quantum wires, Phys. Rev. B 59 (1999) 2267.
[50] K. Masuda, H. Itoh, Y. Sonobe, H. Sukegawa, S. Mitani, Y. Miura, Interfacial giant tunnel magnetoresistance and bulk-induced large perpendicular magnetic anisotropy in (111)-oriented junctions with fcc ferromagnetic alloys: A first-principles study, Phys. Rev. B 103 (2021) 064427.
[51] A.A. Marakushev, N.I. Bezmen, Chemical affinity of metals for oxygen and sulfur, Int. Geol. Rev. 13 (1971) 1781-1794.
[52] P. Lu, F. Cosandey, Dislocation structures at Cu-MgO and Pd-MgO interfaces, Acta Metall. 40 (1992) S259-S266.
[53] B.P. Eftink, A. Li, I. Szlufarska, I.M. Robertson, Interface mediated mechanisms of plastic strain recovery in a AgCu alloy, Acta Mater. 117 (2016) 111-121.
[54] P. Wynblatt, D. Chatain, A.D. Rollett, U. Dahmen, Origin of an unusual systematic variation in the heteroepitaxy of Ag on Ni – The roles of twinning and step alignment, Acta Mater. 168 (2019) 121-132.
[55] J. Wang, A. Misra, J.P. Hirth, Shear response of sigma 3{112} twin boundaries in face-centered-cubic metals, Phys. Rev. B 83 (2011) 064106.
[56] W. Xu, A.P. Horsfield, D. Wearing, P.D. Lee, First-principles calculation of Mg/MgO interfacial free energies, J. Alloy. Comp. 650 (2015) 228-238.
[57] S. Lu, J. Ågren, L. Vitos, Ab initio study of energetics and structures of heterophase interfaces: From coherent to semicoherent interfaces, Acta Mater. 156 (2018) 20-30.
[58] K. Masuda, H. Itoh, Y. Sonobe, H. Sukegawa, S. Mitani, Y. Miura, Band-folding-driven high tunnel magnetoresistance ratios in (111)-oriented junctions with $SrTiO_3$ barriers, Phys. Rev. B 106 (2022) 134438.
[59] F. Bonell, S. Andrieu, C. Tiusan, F. Montaigne, E. Snoeck, B. Belhadji, L. Calmels, F. Bertran, P. Le Fèvre, A. Taleb-Ibrahimi, Influence of misfit dislocations on the magnetoresistance of MgO-based epitaxial magnetic tunnel junctions, Phys. Rev. B 82 (2010) 092405.
[60] T. Scheike, Z. Wen, H. Sukegawa, S. Mitani, Enhanced tunnel magnetoresistance in Fe/Mg_4Al-O_x/Fe(001) magnetic tunnel junctions, Appl. Phys. Lett. 120 (2022) 032404.
[61] R. Shan, H. Sukegawa, W.H. Wang, M. Kodzuka, T. Furubayashi, T. Ohkubo, S. Mitani, K. Inomata, K. Hono, Demonstration of half-metallicity in Fermi-level-tuned heusler alloy $Co_2FeAl_{0.5}Si_{0.5}$ at room temperature, Phys. Rev. Lett. 102 (2009) 246601.
[62] K. Yakushiji, A. Sugihara, T. Nakano, S. Yuasa, Fully epitaxial magnetic tunnel junction on a silicon wafer, Appl. Phys. Lett. 115 (2019) 202403.
[63] T. Nozaki, A. Kozioł-Rachwał, M. Tsujikawa, Y. Shiota, X. Xu, T. Ohkubo, T. Tsukahara, S. Miwa, M. Suzuki, S. Tamaru, H. Kubota, A. Fukushima, K. Hono, M. Shirai, Y. Suzuki, S.

Yuasa, Highly efficient voltage control of spin and enhanced interfacial perpendicular magnetic anisotropy in iridium-doped Fe/MgO magnetic tunnel junctions, NPG Asia Mater. 9 (2017) e451-e451.

[64] G.X. Du, S.G. Wang, Q.L. Ma, Y. Wang, R.C.C. Ward, X.G. Zhang, C. Wang, A. Kohn, X.F. Han, Spin-dependent tunneling spectroscopy for interface characterization of epitaxial Fe/MgO/Fe magnetic tunnel junctions, Phys. Rev. B 81 (2010) 064438.

[65] T. Dimopoulos, G. Gieres, S. Colis, J. Wecker, Y. Luo, K. Samwer, Magnetic tunnel junctions with yttrium oxide barrier, Appl. Phys. Lett. 83 (2003) 3338-3340.

[66] T. Ichinose, T. Yamamoto, T. Nozaki, K. Yakushiji, S. Tamaru, M. Konoto, S. Yuasa, Cryogenic temperature deposition of high-performance CoFeB/MgO/CoFeB magnetic tunnel junctions on ϕ300 mm wafers, ACS Appl. Electron. Mater. 5 (2023) 2178-2183.

Figures and tables

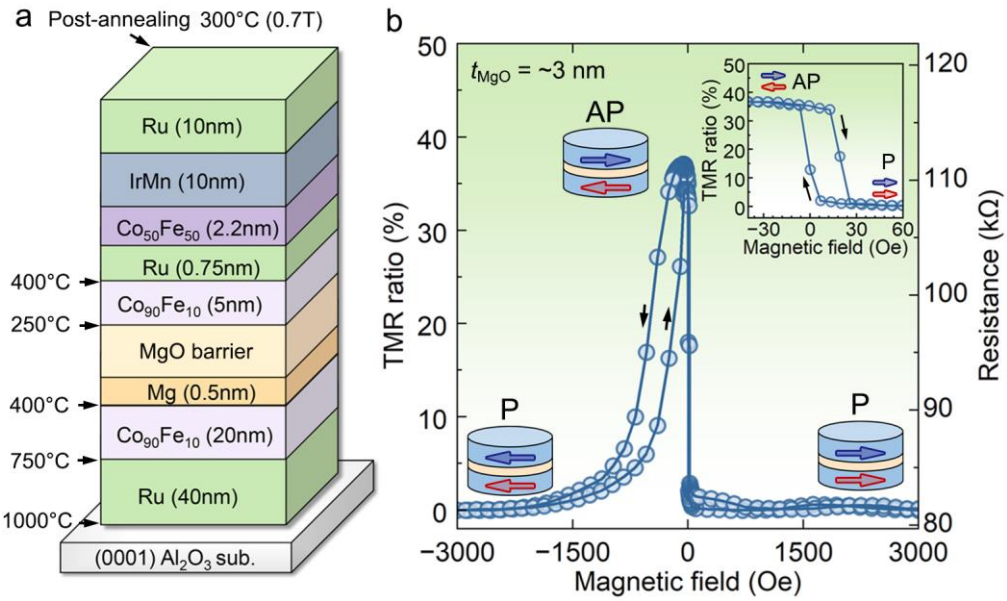

Fig. 1 (a) Schematic stacking structure of the CoFe/MgO/CoFe(111) magnetic tunnel junction (MTJ). (b) Measured TMR ratio vs in-plane magnetic field (*H*) and resistance vs in-plane *H* for a MgO thickness of ~3 nm at a temperature of 300 K. The minor R-H loop in the inset of (b) shows the close-up near the zero field.

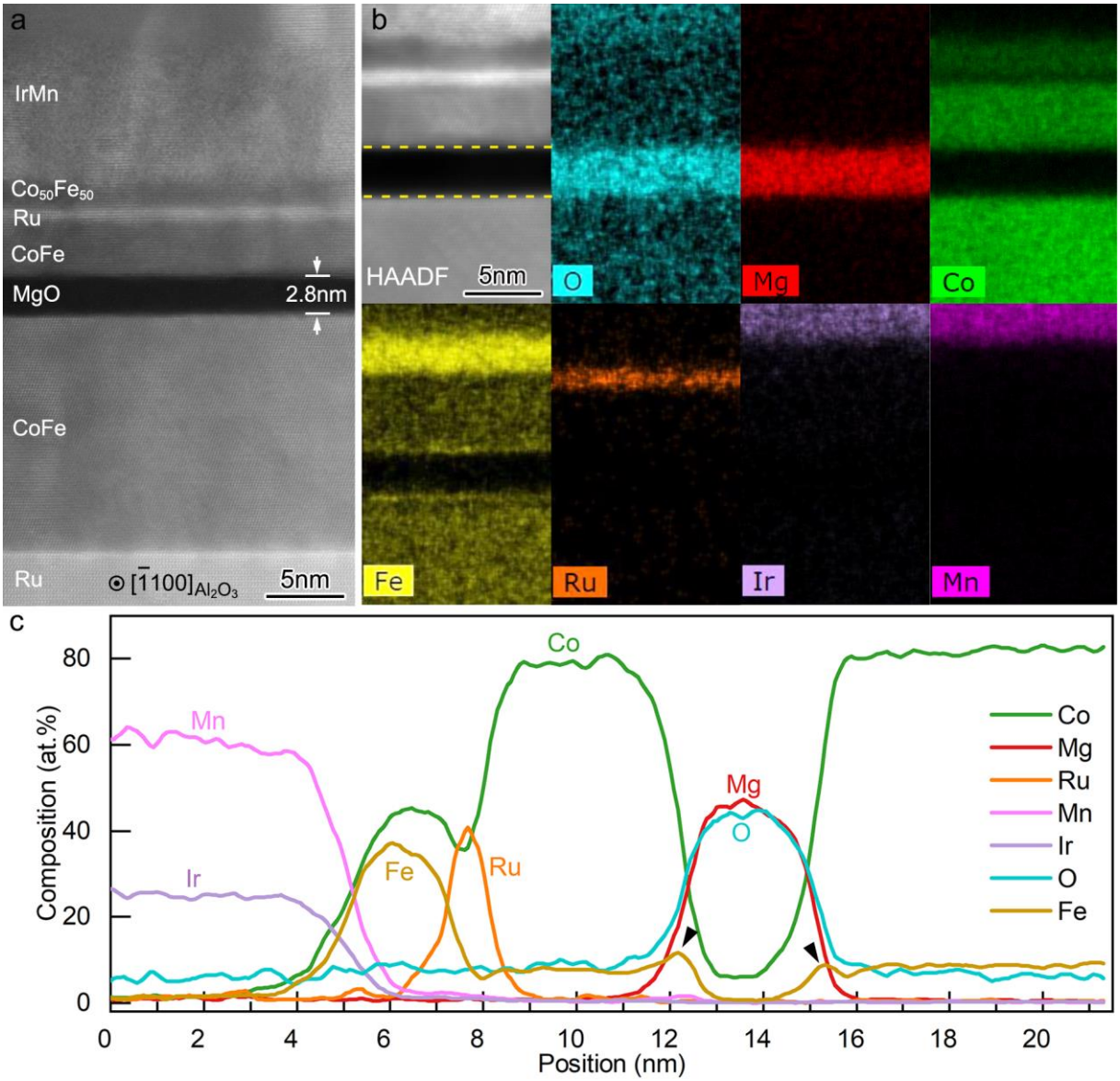

Fig. 2 (a) Low-magnification ADF-STEM image showing the cross-sectional microstructure of the CoFe/MgO/CoFe MTJ with an MgO barrier layer of ~3 nm. (b) EDS mapping analysis of different elements in the CoFe/MgO/CoFe trilayer. (c) Top-to-bottom integrated EDS elemental line profiles generated from EDS maps in (b). The viewing direction is parallel to the $[\bar{1}10]_{CoFe}$ zone axis.

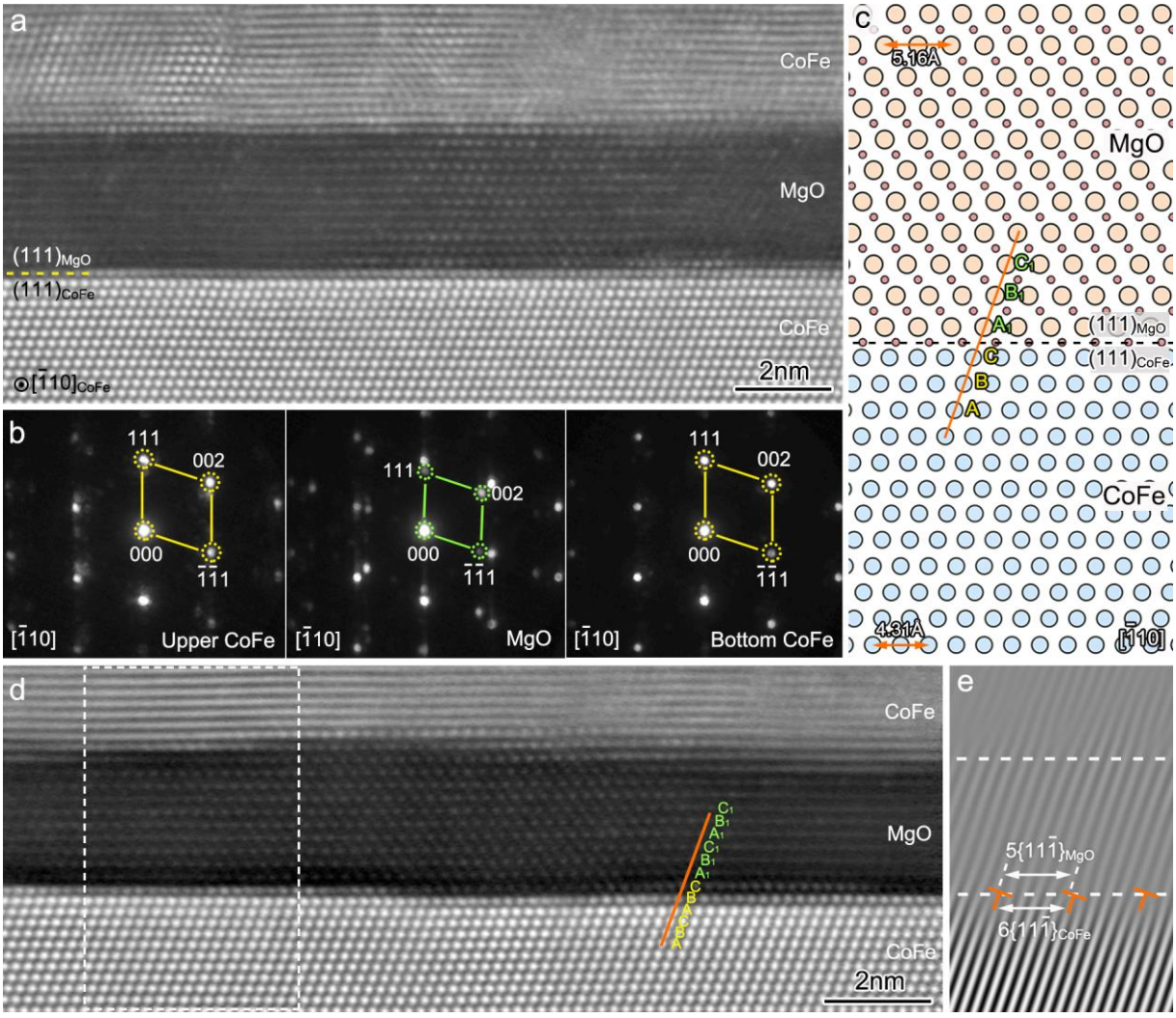

Fig. 3 Type-1 nano domain at CoFe/MgO interface. (a) Atomic-scale ADF-STEM image taken along $[\bar{1}10]_{CoFe}$ showing domain structure in the MgO barrier, where a small MgO crystal grain with a diameter of ~5 nm is revealed. (b) Corresponding NBED patterns collected from the bottom CoFe, MgO barrier and upper CoFe, respectively. (c) Schematic diagram of the lattice match at the CoFe/MgO interface along the direction of $[\bar{1}10]$. (d) Another domain in the MgO barrier, with a larger diameter of ~13 nm. (e) Fourier-filtered image of the region marked by the white dashed-line rectangular frame in (d), showing the periodic distribution of misfit dislocations along the interface between CoFe and MgO. The stacking sequence of close-packed planes for CoFe{111} and MgO{111} are ABCABC and $A_1B_1C_1A_1B_1C_1$, respectively.

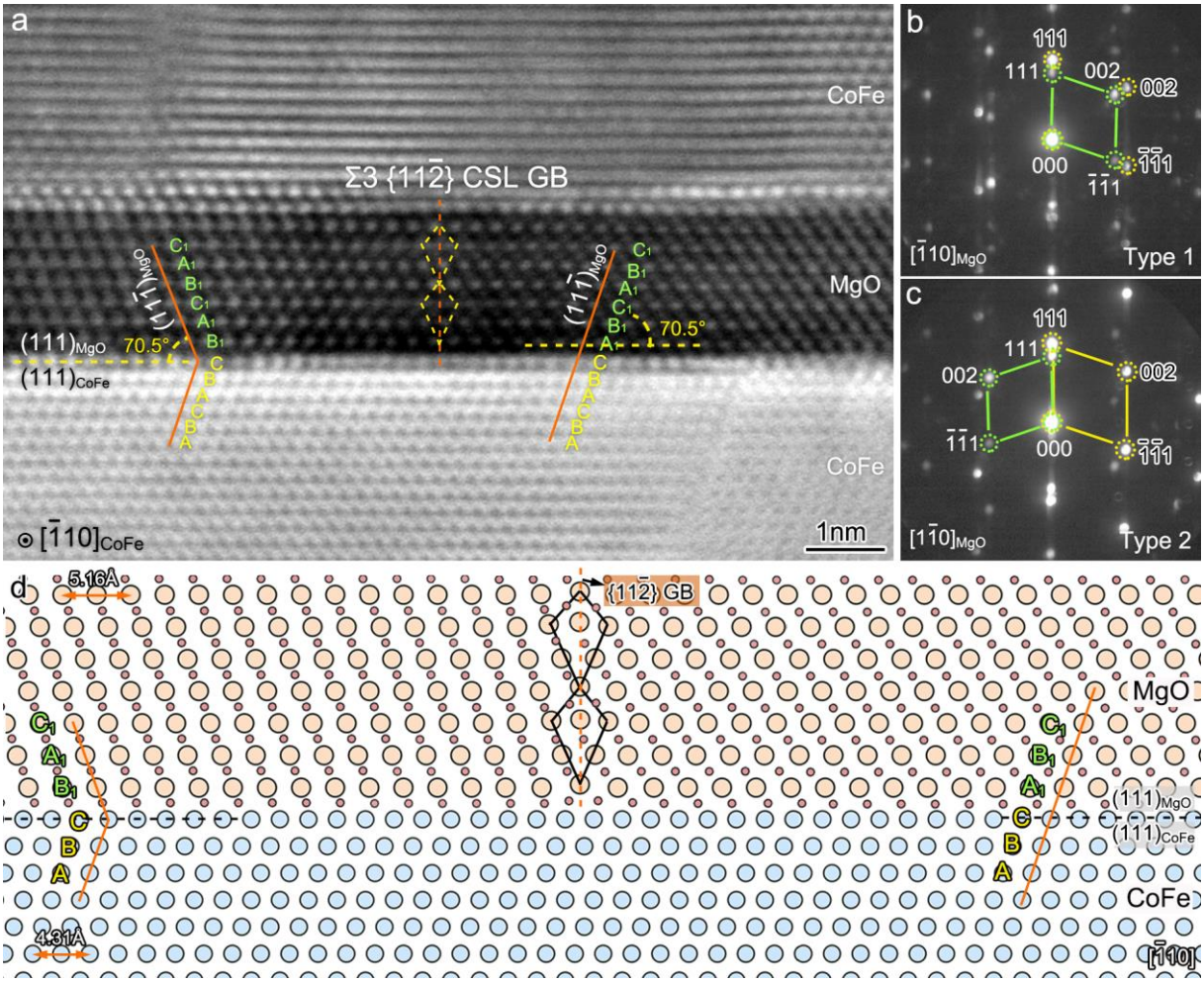

Fig. 4 Type-2 nano domain at CoFe/MgO interface. (a) $[\bar{1}10]_{CoFe}$ ADF-STEM image showing two MgO crystal domains contacting each other. The left one is Type-2 domain and the right one is of Type-1, with a domain boundary of Σ3{112} CSL in between. (b) and (c) are NBED patterns obtained from these two types of domains, respectively. Yellow and green dotted circles represent reflections of CoFe and MgO, respectively. (d) Schematic diagram of the Type-2 domain lattice-matched to the Type-1 domain at the CoFe/MgO interface, with the viewing direction lying parallel to $[\bar{1}10]$.

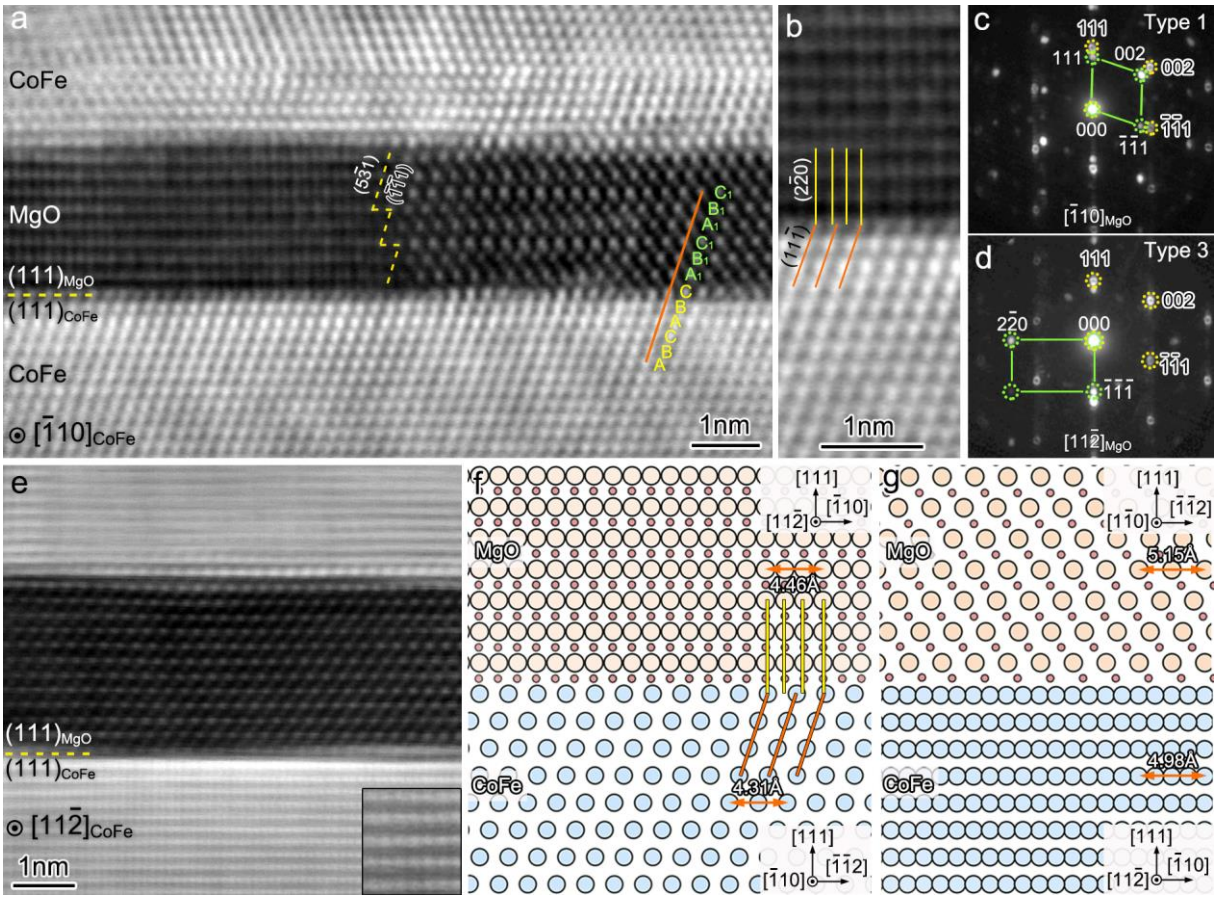

Fig. 5 Type-3 nano domain at CoFe/MgO interface. (a) $[\bar{1}10]_{CoFe}$ ADF-STEM image showing two MgO crystal domains contacting each other. The left one is Type-3 domain and the right one is of Type-1. (b) An enlarged image of Type-3 domain showing a good atomic match between three CoFe$\{11\bar{1}\}$ planes with four $\{2\bar{2}0\}$ planes. (c) and (d) are NBED patterns of these two domains taken along $[\bar{1}10]_{MgO}$ and $[11\bar{2}]_{MgO}$, respectively. (e) ADF-STEM image of the Type-3 domain observed along the $[11\bar{2}]_{CoFe}$ direction. The inset in the lower right is a high-magnification image of CoFe. (f) and (g) are schematic diagrams of Type-3 MgO domain lattice-matched to CoFe along $[\bar{1}10]_{CoFe}$ and $[11\bar{2}]_{CoFe}$ directions, respectively.

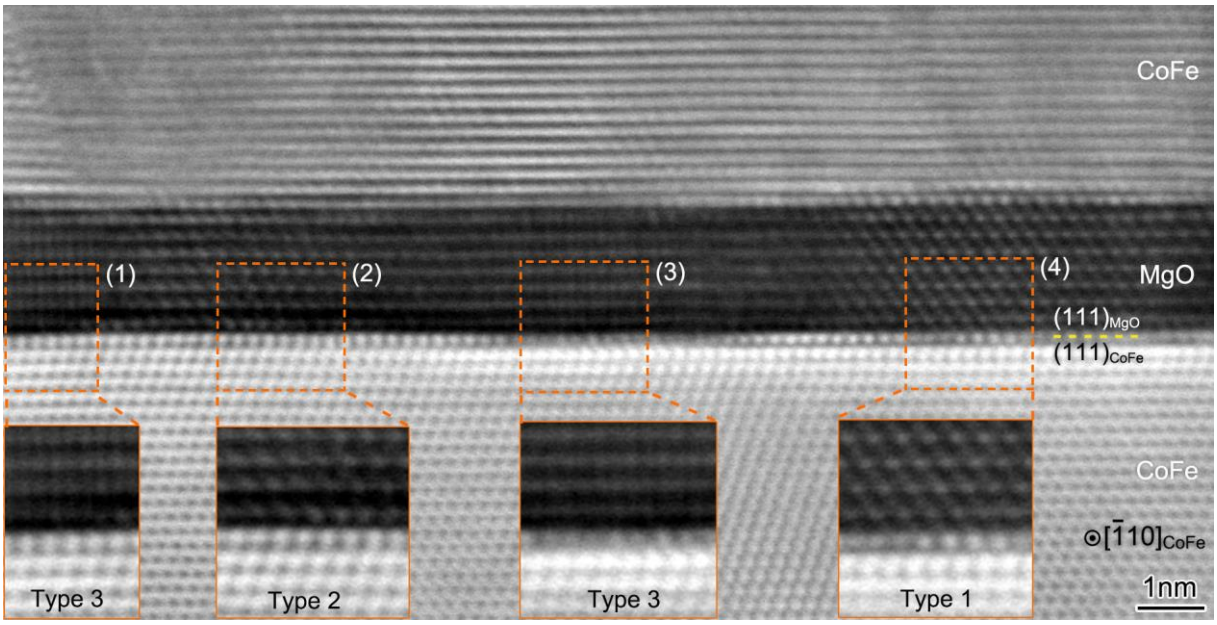

Fig. 6 Representative ADF-STEM image showing multiple nano-domains in the MgO barrier layer, where three types of lattice matching at the CoFe/MgO interface are detected. The electron beam direction is parallel to $[\bar{1}10]_{CoFe}$ direction.

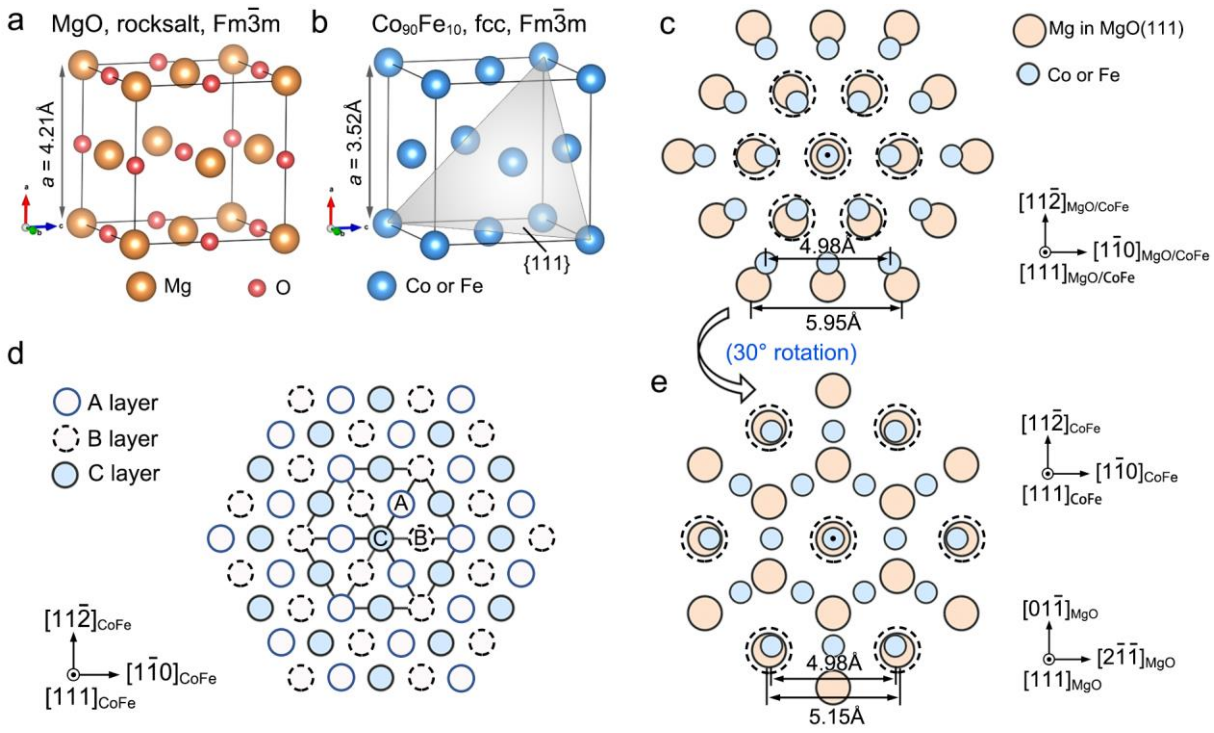

Fig. 7 Formation mechanism MgO domain structures with three types of lattice matching at the CoFe/MgO (111)-oriented interface. (a-b) Schematic diagrams of rocksalt MgO and fcc CoFe lattices, respectively. (c) and (e) are in-plane atomic matching between CoFe(111) and MgO(111) planes for Type-1 and Type-3 MgO domain structures. 30° in-plane rotation of the MgO lattice with respect to Type-1 orientation between CoFe and MgO leads to the formation of Type-3 OR. (d) Atomic arrangements of CoFe viewed along [111] direction. Three different close-packed {111} planes that could be readily distinguished along the projection direction are represented by A, B and C, respectively.

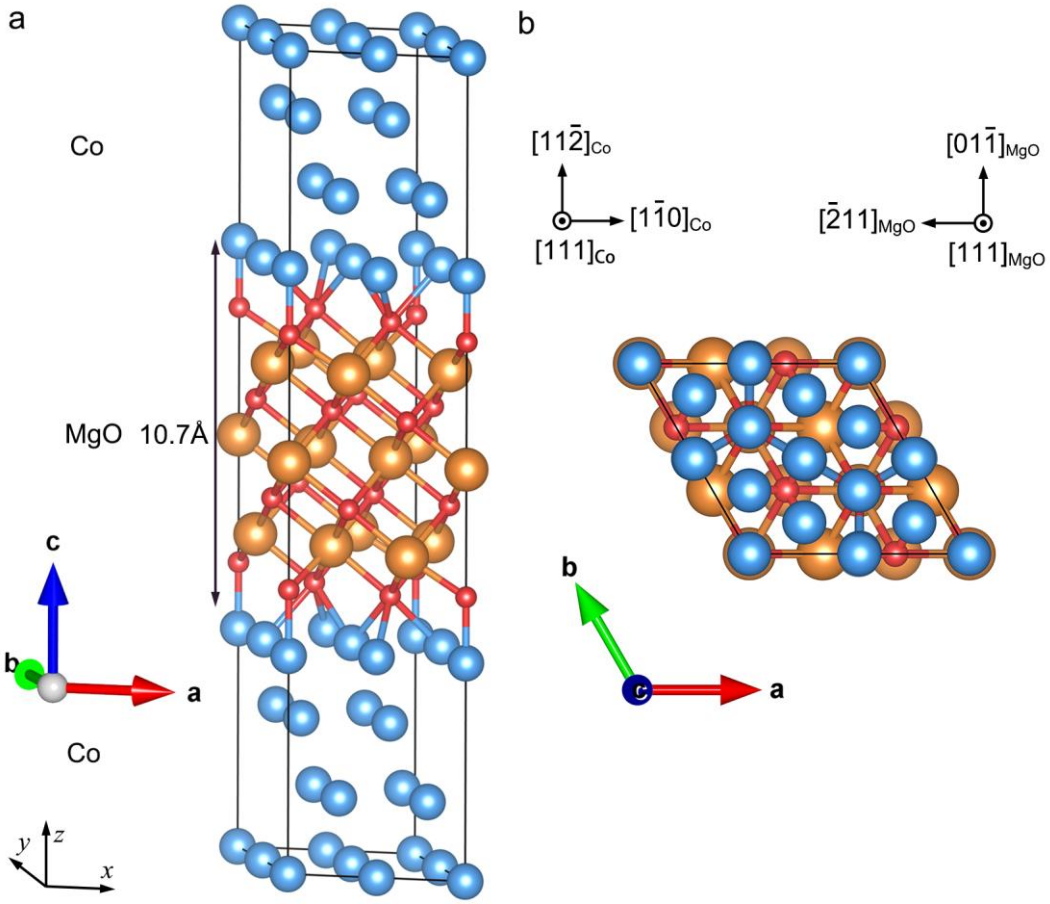

Fig. 8 Calculation supercell of the Type-3 Co/MgO/Co (111)-oriented MTJ: (a) three-dimensional model and (b) [111]-projected atomic model.

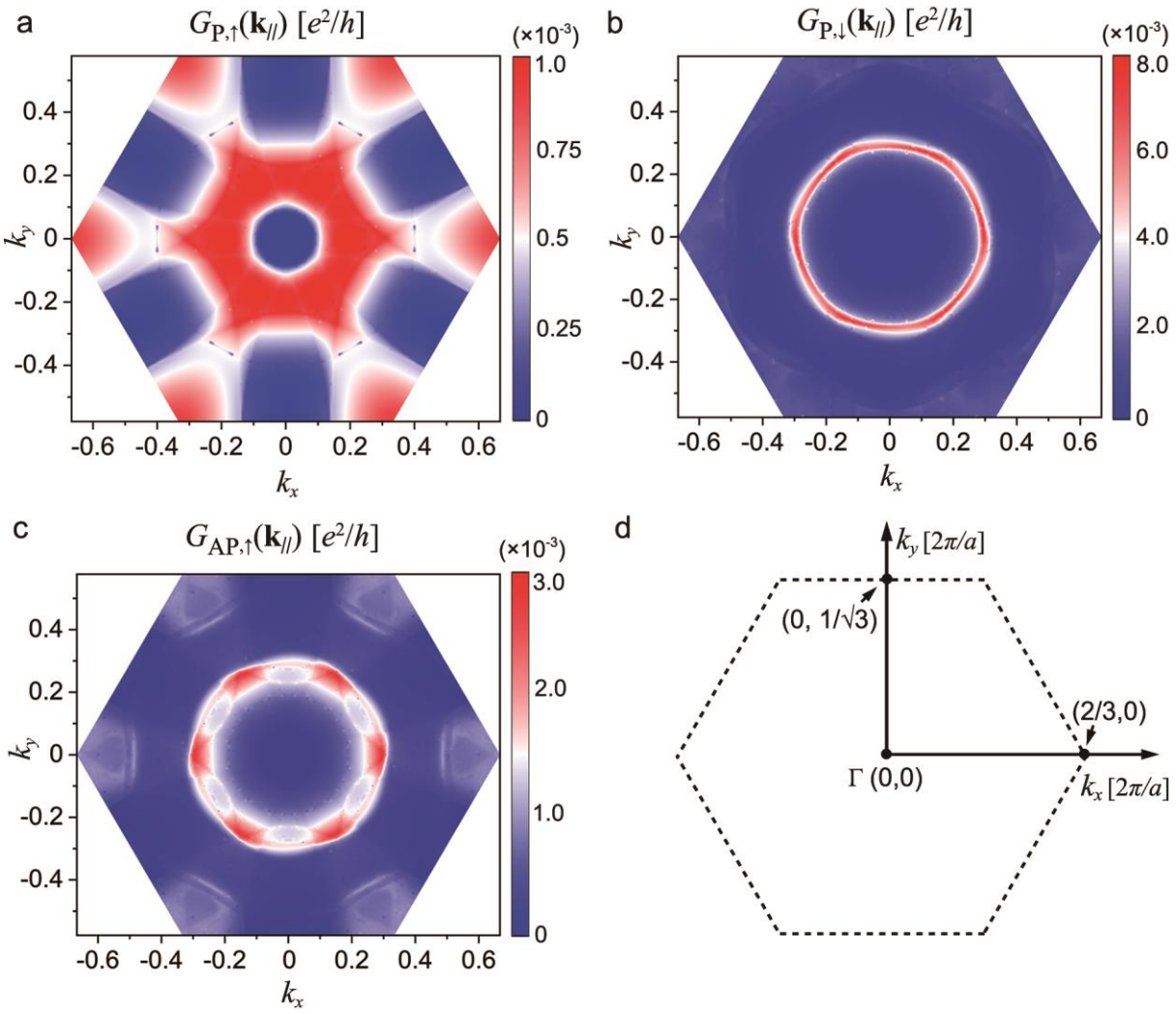

Fig. 9 (a-c) Calculated $\mathbf{k}_{||}$-resolved majority- and minority-spin conductances in the parallel and antiparallel configurations of magnetizations. (d) Coordinate of the two-dimensional Brillouin zone for calculation.

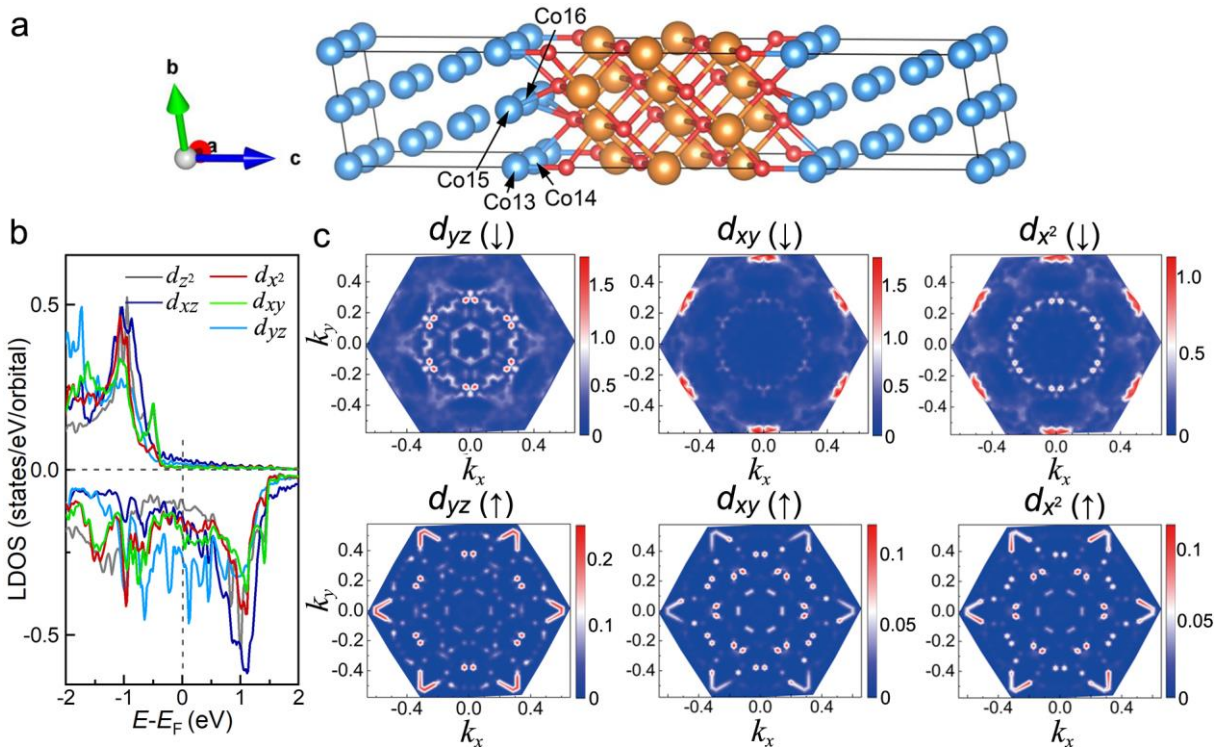

Fig. 10 Local density of states (LDOSs) of interfacial Co atom at Co/MgO interface with a Type 3 orientation. (a) 3-dimensional Type-3 Co/MgO/Co (111)-oriented junction. (b) Projected LDOSs of the interfacial Co atom where d_{x^2} and d_{z^2} stand for $d_{x^2-y^2}$ and $d_{3z^2-r^2}$, respectively. (c) The $\mathbf{k}_{\parallel}$-resolved LDOSs of the interfacial Co atom at the Fermi energy level.

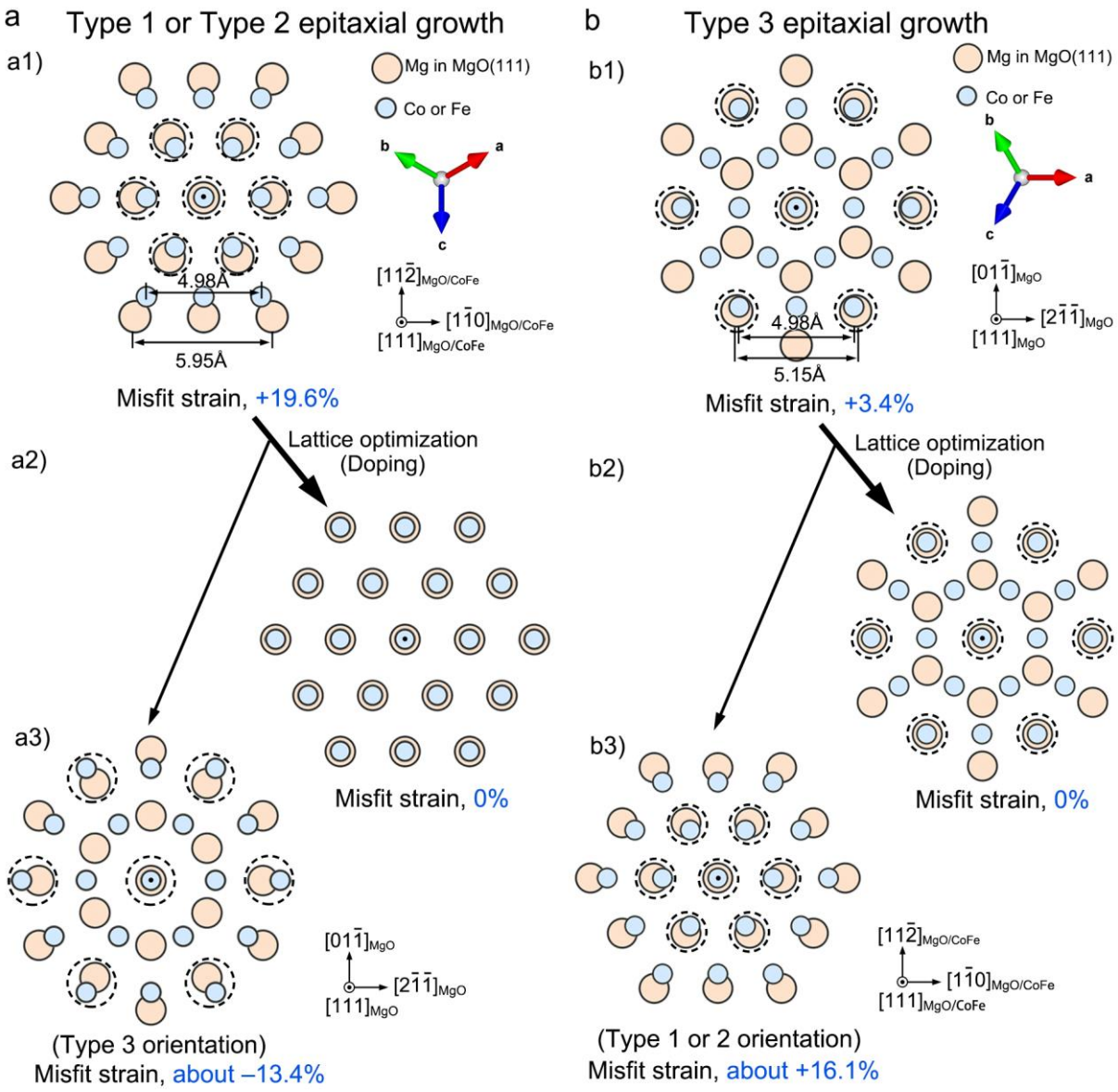

Fig. 11 Future rational design of fully epitaxial (111)-oriented MTJ devices using the method of atomic doping: (a) Type-1 or Type-2 (111)-oriented MTJ and (b) Type-3 (111)-oriented MTJ.

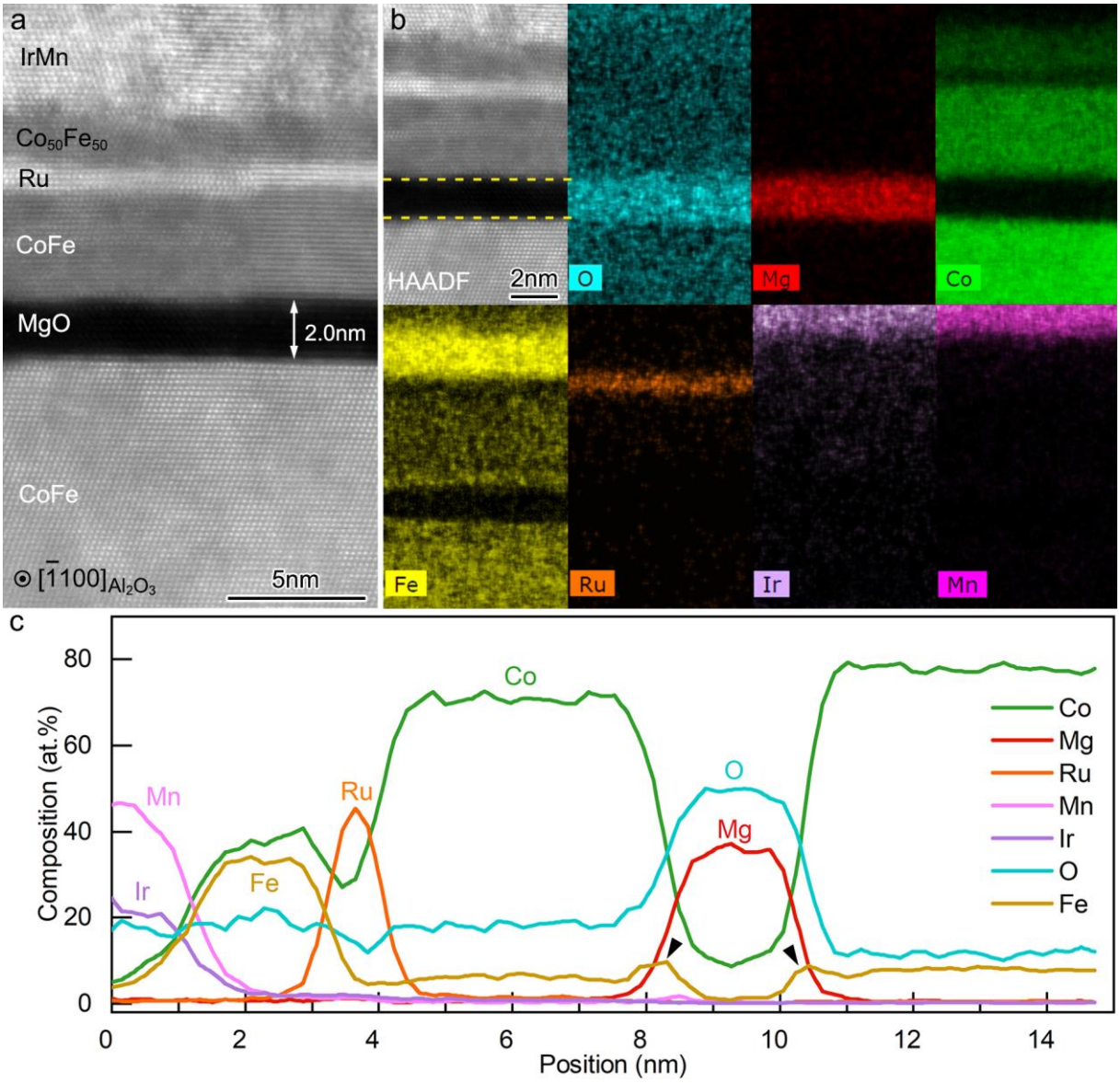

Fig. 12 Observation of a region in an MTJ with over-oxidized MgO barrier (thin MgO of 2 nm). (a) Cross-sectional microstructure. (b) EDS mapping analysis of different elements adjacent to the MgO barrier. (c) Top-to-bottom integrated EDS elemental line profiles generated from EDS maps in (b). The electron beam direction is parallel to $[\bar{1}10]_{CoFe}$.

Table 1 Calculated conductances and TMR ratios of the Type-3 and Type-1 oriented Co/MgO/Co(111) MTJs. The unit of conductance is e^2/h.

	Type-3 Co/MgO/Co(111)	Type-1 Co/MgO/Co(111) [37]
$G_{P,\uparrow}$	3.79×10^{-4}	2.48×10^{-3}
$G_{P,\downarrow}$	1.07×10^{-3}	1.42×10^{-3}
$G_{AP,\uparrow}$	6.22×10^{-4}	8.73×10^{-5}
$G_{AP,\downarrow}$	6.22×10^{-4}	8.75×10^{-5}
G_P	1.45×10^{-3}	3.90×10^{-3}
G_{AP}	1.24×10^{-3}	1.75×10^{-4}
TMR	17%	2130%